The Pennsylvania State University

The Graduate School

College of Engineering

DYNAMIC-MESH TECHNIQUES FOR UNSTEADY MULTIPHASE SURFACE-SHIP HYDRODYNAMICS

A Thesis in

Mechanical Engineering

by

Gina M. Casadei

Submitted in Partial Fulfillment
of the Requirements
for the Degree of

Master of Science

December 2010

The thesis of Gina M. Casadei was reviewed and approved* by the following:

Eric G. Paterson
Professor of Mechanical Engineering
Division Scientist, Computational Mechanics Division, Applied Research Lab
Thesis Adviser

H.J. Sommer III
Professor of Mechanical Engineering
Thesis Reader

Karen A. Thole
Professor of Mechanical Engineering
Head of the Department of Mechanical Engineering

* Signatures are on file in the Graduate School

ABSTRACT

Accurate prediction of transient loads and dynamic response, particularly in high sea states, is of crucial importance when designing ships. Computational Fluid Dynamic (CFD) simulation of dynamic, full-scale, three-dimensional bodies in waves is very challenging and computationally expensive, and empirical seakeeping models are often inaccurate under certain conditions. In naval hydrodynamics, there is a need for robust and fast dynamic-meshing methods appropriate for analyzing maneuvering and seakeeping of ships. CFD methods need to be developed to validate viscous roll-damping models, since the ones used in seakeeping codes have been strictly empirical in the past.

A validation study was performed to set the frame-work for understanding viscous dominated flows. These simulations included basic steady and unsteady boundary layer flows for a flat plate and ship-hull geometries. It is critical to prove that the flow solvers are capable of resolving the physics of oscillating flows, boundary layers, and phase lags. The Spalart-Allmaras turbulence model was used for these turbulent flow computations.

Four types of dynamic-meshing techniques were selected to study. Dynamic-overset meshing will be compared to three other techniques: dynamic remeshing via solution of a Laplace equation; dynamic remeshing using radial-basis functions (RBF); and mesh motion and dynamic remeshing using a generalized grid interface (GGI). An analysis of the four types of dynamic-meshing techniques was done by quantifying the accuracy, robustness, stability, and speed of each one. While dynamic remeshing via solution of

a Laplace equation was robust and GGI was the fastest, overset meshing was found to be the most stable and the most general technique for complex geometries and motions. RBF proved to be too computationally expensive and unrealistic for three-dimensional problems. These methods will be validated with recent experimental data that has been collected at the Naval Surface Warfare Center, Carderock Division (NSWCCD) for a two-dimensional, tumblehome section. Simulation results focus on prescribed roll motion in unsteady, two phase flow. This thesis was completed using OpenFOAM and the foamedOver library, the latter of which is a bridging tool that links SUGGAR and DiRTlib to OpenFOAM for overset meshing.

TABLE OF CONTENTS

LIST OF TABLES

LIST OF FIGURES

ACKNOWLEDGEMENTS

First and foremost, I would like to thank my parents for their unwavering encouragement and support. Without them, I would not be where I am today. Throughout every hurdle and obstacle I have encountered in my life, they have been there for me. My mom has always been my best friend and my dad has been my biggest advocate. I want to thank my brother for providing me with his optimistic look on life and the ability to always make me laugh. Graduate school has been a life-changing and defining time in my life and I was able to rely on my colleagues and friends every step of the way. I have made life long friendships. I would like to express my sincere gratitude to my advisor, Dr. Eric Paterson. He has provided me with a second chance at completing research and successfully achieving this degree. I will remember his wisdom and he has left an everlasting impression on me. I would also like to acknowledge Ms. Diane Segelhorst for sponsoring the NAVSEA 073R Graduate Student Program, as well as Dr. Jack Lee and Mr. Chris Bassler as my Navy mentors. The experimental results were supported by Dr. John Barkyoumb, under the Naval Innovative Science and Engineering Program at NSWCCD.

Chapter 1

Introduction

1.1 Motivation

It is crucial to the design of ships to know the transient loads that are possible, as well as the damage that can occur at high sea states. In the past, our understanding of the hydrodynamics of ships has been obtained through empirical data. Viscous roll-damping models are empirical but we need Computational Fluid Dynamics (CFD) to help develop and validate better models. However, CFD simulations of dynamic, full-scale, three-dimensional bodies in waves is very challenging. In naval hydrodynamics, there is a need for robust and fast dynamic-meshing methods appropriate for analyzing maneuvering and seakeeping of ships. These mesh-motion techniques will enable CFD simulations of large amplitude motions to capture the correct flow physics.

There are numerous applications that would benefit from the ability to predict hydrodynamic loads. These applications would include wave-slap and loads on structures, dynamic stability of floating bodies and ships, and water on the decks of ships. Not only is it important to predict the hydrodynamic loads on free-surface ships, but also for surfaced submarines, appendages and installed adjunct vehicles.

1.2 Objective

There are certain components that are needed for the physics based CFD models to predict loads that ships experience at sea. These components include multiphase Reynolds Averaged Navier-Stokes (RANS), six Degrees of Freedom (DOF) solver, wave models, and dynamic meshing. This thesis will analyze and quantify the performance of four dynamic mesh-motion techniques for free-surface ship-hydrodynamics during large amplitude roll motion. These dynamic-meshing methods include dynamic motion via solution of Laplace equation, Radial Basis Function (RBF), Generalized Grid Interface (GGI), and overset. These methods' performance will be quantified by speed, accuracy, robustness, and stability. This thesis will also be validated by recent experimental data from a two-dimensional (2D) ship tumblehome hull section. The performance of standard turbulence models in OpenFOAM for unsteady boundary layer flows on flat plate and ship-hull geometry will also be evaluated.

1.3 Literature Review

1.3.1 History

In the past, empiricism has controlled the advances of ship-hydrodynamics. It is very common to use the equations of motion with experimentally determined coefficients to simulate the dynamic behavior and controllability of a ship in various conditions. The experimentally determined coefficients are computed through a planar motion mechanism

and rotating arm model tests. These simulations can then be used to select rudder sizes and steering control systems [15].

Potential flow analysis would be advantageous over experimentation when it comes to determining coefficients, except that it is inaccurate. The hull forces are difficult to predict due to the sway and yaw as well as shedding of strong vortices that occur during a turn. When the rudder is in the hull boundary layer, viscous effects are dominant, and therefore, potential flow analysis can not accurately predict maneuvering coefficients.

Morgan [15] expects that as RANS codes become more robust, less effort will be placed on determining coefficients through experimentation and more effort will be placed on numerical predictions.

1.3.2 Seakeeping

The ocean is a very dynamic, unsteady and unpredictable body of water. Waves can be described as changing in space and time since the primary generating mechanism is wind. Waves can also be described as being stochastic in nature. Ship-hydrodynamics become very complex with the uncertainty of wave patterns, which establishes a need for advanced research in this area. Ship dynamics are generally divided into two areas: maneuvering and seakeeping. Maneuvering refers to the controllability in calm water with six DOF, and seakeeping refers to the vessel motion in a seaway [19], where a seaway is a body of water containing waves. This thesis is concerned with seakeeping and maneuvering. Linear equations of motion are used to describe the ships response to wave excitation loads during seakeeping. The power spectrum of six DOF are obtained

and the seakeeping analysis can be completed. The equations of motion, with theory based coefficients [19], are given by

$$\sum_{k=1}^{6}[M_{ik} + A_{ik}(\omega_e)]\ddot{\eta}_k + B_{ik}(\omega_e)\dot{\eta}_k + C_{ik}\eta_k = \tau_{Wk} \; for \, i = 1, ...6$$

where M_{ik} are the rigid body generalized mass coefficients, $A_{ik}(\omega_e)$ are the added mass coefficients, $B_{ik}(\omega_e)$ are the potential and equivalent linearized viscous damping coefficients, C_{ik} are the linear restoring coefficients, τ_{Wk} is the wave excitation forces, and ω_e is the wave encounter frequency domain. However, potential theory cannot be used to compute roll damping moments due to the strong viscous effects that are present [20]. These equations are solved in the frequency domain for sinusoidal wave excitation, however, the models are not accurate at low frequencies.

1.3.3 Ship Motion and Roll Damping

Ship motions can be divided into two types: translational (heave, sway, and surge); and rotational (pitch, roll, and yaw). Pitch and roll are the most violent and have the greatest effects on the human body. Roll is dominated by viscous effects and is difficult to predict. Pitch is dominated by lift effects or buoyancy and is uncomplicated as long as the seaway is well prescribed [15].

Himeno states "that good predictions of ship motions in sway, yaw, heave, and pitch can be made if little is known about the ship and seaway" [11] . However, this is not the case

for roll motion. Roll motion is one of the most difficult, but responses to roll motion are important to predict in a body of water. It is sensitive to fluid viscosity unlike heave, pitch, sway and yaw. Bilge keels are difficult to analyze, but greatly influence the roll motion of a ship. The behavior of a ship in the ocean during high sea states is more difficult to understand due to nonlinear characteristics [11].

There are many contributions to the moments acting on a ship, but the most crucial is the roll damping moment. The roll damping moment is needed to secure the safety of a ship at the initial stage of design, as well as to understand the ship motions in waves. Roll motion of a ship in simple single DOF form is:

$$A_\phi \ddot{\phi} + B_\phi \ddot{\phi} + C_\phi \ddot{\phi} = M_\phi(\omega t) \tag{1.1}$$

where ϕ is the roll angle, A_ϕ is the virtual mass moment of inertia along a longitudinal axis through the center of gravity, B_ϕ is the roll damping moment, C_ϕ is the coefficient of restoring moment, M_ϕ is the exciting moment due to waves or external forces acting on the ship, ω is the radian frequency, and t is time.

Ikeda developed a method for predicting the roll damping of a ship over twenty-five years ago. Ikeda states "that the roll damping generated by the bilge keels is determined by integrating the pressure distribution over the bilge keels and hull surface" [12]. The method was composed of five components: friction, wave, eddy, lift and bilge keel components [12]. Since then, the method has been modified by accounting for the exact cross section and exact location of the bilge keels, and forward speed effect on the bilge keels. Also,

the eddy component of the roll damping is more accurately predicted by using a formula that places the center of gravity above the water surface.

1.3.3.1 Roll Motion

Yeung [30] studied the forced-motion hydrodynamic properties of rectangular cylinders fitted with bilge keels with two different Navier-Stokes solvers. It was found that an increase of roll amplitude reduces the nondimensional inertia coefficients slightly, but increases the damping coefficients appreciably. Bangun [9] studied a rectangular cylinder subjected to forced rolling at the free-surface and was able to accurately predict the cyclic nature of vortex generation and pressure contours around the rolling cylinder. A harmonic oscillation of $\theta = \theta_a sin\omega t$ was prescribed to the rolling cylinder. However, at larger angular amplitudes, the pressure-correction equation remained a challenge to solve.

1.3.3.2 Large Amplitude Roll Motion

Bassler, *et al.* [1] conducted an experiment to quantitatively characterize changes in the system conditions and behavior for a ship-hull section experiencing large amplitude roll motion. Bassler stated "that this research would help with considerations in the development of a ship roll damping model to predict ship behavior in heavy weather" [1]. Bassler used a two-dimensional model to represent the midship section of the Office of Naval Research (ONR) Topside Series hull forms and performed experiments in the 140 ft basin at NSWCCD. A series of roll amplitudes and frequencies were tested with one DOF,

which was the roll component. At the higher amplitudes, the bilge keels emerged from the free-surface and water shipping occurred, which is when water is located on top of the bilge keel during emergence. Slap occurred during re-entry, causing air-entrainment on the underside of the bilge keels. When the bilge keels became fully submerged again, vortex shedding resulted around the tip of the bilge keels. Increased load developed when a previously shed vortex interacted with the bilge keel, while a new vortex was being generated. Bassler stated "that the results of this research can be used in the sectional-based theoretical formulations to predict ship roll motion behavior" [1].

The first step in assessing the validity of the body-exact strip-theory based method for use within the naval hydrodynamics community is characterization of ship performance in high sea states. Belknap, *et al.* [25] studied the effects of changing the ship-hull geometry to see if there was an effect on the hydrodynamic coefficients. The main challenge of this research was characterization of the operational risk of operating in sea states that lead to extreme ship motions and loads. This experiment was conducted with a two-dimensional ship-hull model and compared with results from OpenFOAM. An upright heave motion without bilge keels was tested and results indicated that the RANS calculations match closely with the potential flow calculations. It was found that for large amplitude, low frequency cases, the hydrostatic force represents the majority of the total force. Also, for the higher frequency cases, more nonlinearities were present in the hydrodynamic forces. The next phase of research needed for body-exact models is to expand the validation cases to include pitch motion, waves, multiple DOF, and horizontal modes of motion.

1.3.3.3 Bilge Keels

Typically for large amplitude roll motion, the amount of energy dissipation is over estimated which results in under prediction of the roll motion. The primary mechanism for roll damping on ships is bilge keels, which makes bilge keels of significant importance. Bilge keels were originally designed for small to moderate roll motion, but now ships are entering more extreme conditions that man previously avoided. When bilge keels interact with the free-surface, this is where the roll damping is over-predicted and needs to be studied further.

Bilge keels are welded on each side of a ship, along the length to increase hydrodynamic resistance to rolling. Bilge keels increase flow separation and vortices generated off the sharp edges of the keels, which ultimately increase the damping force on a barge or ship. Bangun [9] studied the hydrodynamic forces on a rolling barge with bilge keels and found that horizontal bilge keels provide better roll damping coefficients than bare hulls. He also found that the best inclination of the bilge keels is found where the roll center of the barge joins the corner of the barge. Another important conclusion Bangun stated was that when the angular amplitude of the roll motion is increased, so is the severity of flow separation, creating more effective roll damping [9].

1.3.4 Unsteady Viscous Flow

Obtaining accurate experimental data from ship motions in unsteady viscous flow during forward speed is a challenge. Therefore, simulations of this motion, which involve cross-flow over a ship, would be easier to test. These studies are more prevalent and involve oscillating flow while keeping an object of interest stationary.

Choi [8] studied the flat plate laminar boundary layer with an oscillatory external flow, creating a temporal wave, shown in equation (1.2).

$$U_e = U_1 cos(\xi t) \tag{1.2}$$

Where ξ is the frequency of oscillation. A wide range of parameters were considered and tested at Re = 10^4. This study displayed all the well known features expected, such as velocity overshoots, phase leads and streaming. The results show a small disturbance to the steady solution, in terms of ξ. This thesis will also examine first-harmonic overshoot values for oscillatory external flow.

Sarpkaya [21] studied sinusoidally oscillating flow about a cylinder in viscous fluid and used the Morison Equation to back out C_d and C_m values from his experiment. He evaluated in-line force data on cylinders over a range of β values using a U-shaped water tunnel to perform oscillatory flow experiments. He found that theoretical values of the inertia coefficients agree with the values obtained experimentally for Keulegan-Carpenter

numbers before boundary layer transition. The drag coefficient predicted by the Stokes-Wang analysis agree well with the values obtained experimentally for values of K less than K_{cr}, which is when the flow becomes unstable.

1.3.5 CFD

There are three key areas to CFD: algorithm development, grid generation and turbulence modeling. Turbulence modeling is a mathematical model that approximates the physical behavior of turbulent flows. However, if a proper grid is not created, the turbulence modeling will be inaccurate. The grid must be refined in the proper locations to be useful to the simulation. Since gridding is so important to the completion of a simulation, the type of grid used is just as significant. Below, the tools used in this thesis are discussed.

1.3.5.1 OpenFOAM

OpenFOAM (Open Field Operation and Manipulation) is the CFD tool used in this thesis and is licensed under the General Public License (GNU). It is a C++ object-oriented library for numerical simulations in continuum mechanics. OpenFOAM is a finite volume code that solves systems of partial differential equations. The PDE's are discretized and a system of linear equations are ultimately solved using a specified method (Gauss-Seidel, Jacobi, *etc.*) based on cell centered values. The available solvers and libraries for this code has steadily grown as the amount of users and developers has increased. The solvers range from solving multiphase flows to compressible and incompressible flows, as well as solving combustion and electromagnetic problems. There are meshing tools available for

pre-processing such as Pointwise and Gridgen, and tools available for post-processing such as ParaView.

1.3.5.2 Grid Generation

When preparing a grid to import into a CFD code, the choice of grids is essential to the overall success of the simulation. There are three basic grid types that can be selected: structured-Cartesian, structure body-fitted or unstructured (tetrahedral, hexahedral or prismatic) [29]. This thesis will only examine grids that are structure body-fitted because they are relatively simple to generate, and allow for a boundary layer mesh to surround the areas with large velocity gradients.

1.3.6 Dynamic Mesh Techniques

1.3.6.1 Laplacian Mesh Morphing

A computationally robust dynamic-mesh technique used in CFD is Laplacian mesh morphing, which solves a Laplace equation to move the mesh. Bos [3] used this method along with solid body rotation stress to compare with radial basis function interpolation while studying insect flight. Bos found that the Laplace equation method was not able to maintain high mesh quality around the boundary of a rectangle when it rotates, shown in Figure 1.1. The cell skewness in the domain is highest near the body, while the remaining mesh is relatively unaltered.

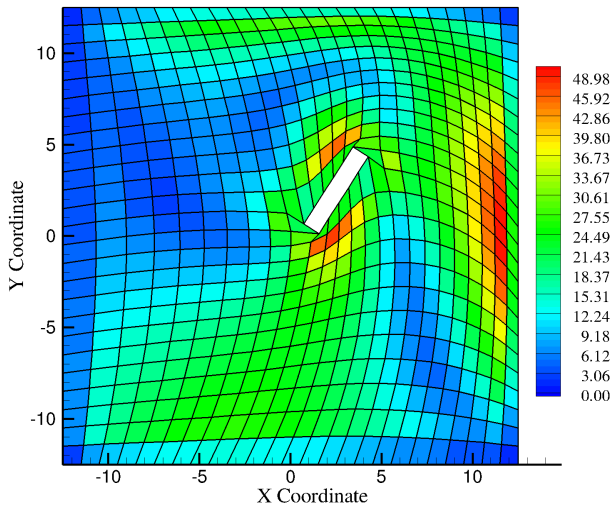

Figure 1.1: Cell non-orthogonality of Laplace mesh motion solver

Smith also used Laplacian mesh morphing for prescribed roll oscillation of a tumblehome midship geometry [23]. He analyzed a ship-hull section with and without bilge keels at several amplitudes and frequencies. He found that at larger roll amplitudes, the mesh quality decreased significantly. However, the method remained quite robust even with the complex geometry and high amplitude mesh motion.

1.3.6.2 Radial Basis Function

A common problem in CFD is maintaining high mesh quality during large transformations and rotations, as shown in the Laplace equation method above. One mesh technique that can handle large mesh deformations is based on the interpolation of radial basis functions (RBF). This technique can offer superior mesh motion in terms of mesh quality on average but can be computationally expensive. It is critical when using RBF that

the mesh quality remains high. If the worst mesh quality is too low, the simulation will diverge. However, if the mesh quality remains high, the simulation will remain stable, accurate and efficient. Bos [3] studied the wing performance for flapping wings of insects at small scales. The RBF method can handle this motion by interpolating the displaced boundary nodes on the surrounding mesh. Bos also studied the difference between using the Laplace equation with variable diffusivity, solid body rotation stress equation and RBF. The skewness and non-orthogonality values were compared for all cases and the RBF showed higher mesh quality for both skewness and non-orthogonality.

Figure 1.2 clearly displays that the RBF deforms around the rotating rectangle, unlike the Laplacian mesh motion (Figure 1.1) which has highly skewed cells around the rectangle. In Figure 1.2, the mesh deformation of SBR Stress and RBF are compared. The high mesh quality is more preserved in regards to RBF compared to SBR. However, RBF requires much more computational effort between iterations during the mesh update scheme, which is a huge downfall to this method.

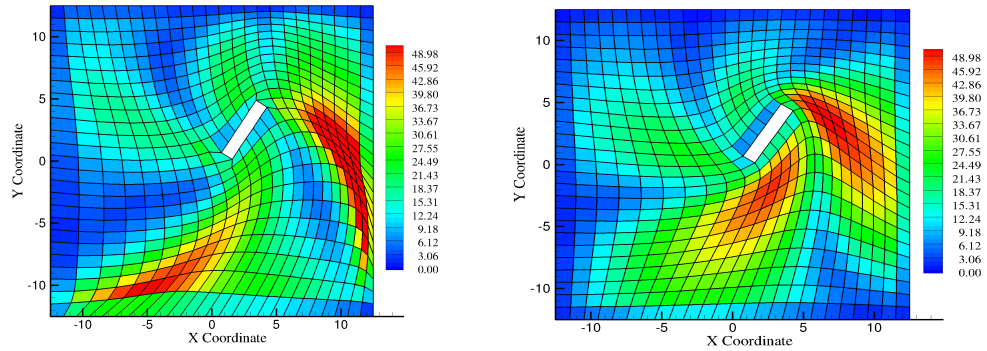

(a) SBR Stress

(b) RBF

Figure 1.2: Mesh Deformation of SBR Stress and RBF mesh motion

1.3.6.3 Generalized Grid Interface

Generalized Grid Interface (GGI) refers to a grid on either side of two connected surfaces, where the grid connectors do not have to match. GGI connections allow non-matching of nodes which can be beneficial for many reasons. The main advantage to this meshing technique is that it does not have to adapt the topology of the mesh at the interface between two non-conformal meshes [2]. Each of the GGI regions can be different sizes, but cannot have overlap regions. One paper studies the use of a GGI for the application of turbomachinery [2]. GGI can be described as using weighed interpolation to evaluate and transmit flow values over patches in the mesh. These flow values are controlled from the master patch to the shadow patch through a set of finite volume method discretization reasoning.

The downfall to this method is that even with minimal error in the master patch variable, unacceptable discretization error can occur [2]. The GGI weighting factors relate to the percentage of surface intersection between two overlapping faces. The GGI method uses the Sutherland-Hodgman algorithm in OpenFOAM to compute the master and shadow face intersection surface area. This algorithm must be used with convex polygons only, which could cause problems with complicated geometries where non-convex polygons are present. Inaccuracies can also occur at the border between a rotating and fixed part of the mesh due to possible gaps between the faces.

1.3.6.4 Overset Methods

One method of grid generation that has many advantages is an overset-grid approach. This process involves constructing several blocks that are overlapping, made up of structured or unstructured grids. Partial differential equations are solved on each component and boundary information is then exchanged between these grids based on interpolation [22]. The unused grid points are cut from the solution known as hole points. The points that are overlapped between grids are known as fringe points. The interpolation points are identified as the points that interpolate between the overlapped grids to obtain a solution [7]. Figure 1.3 shows an example of a boundary layer grid and a background grid.

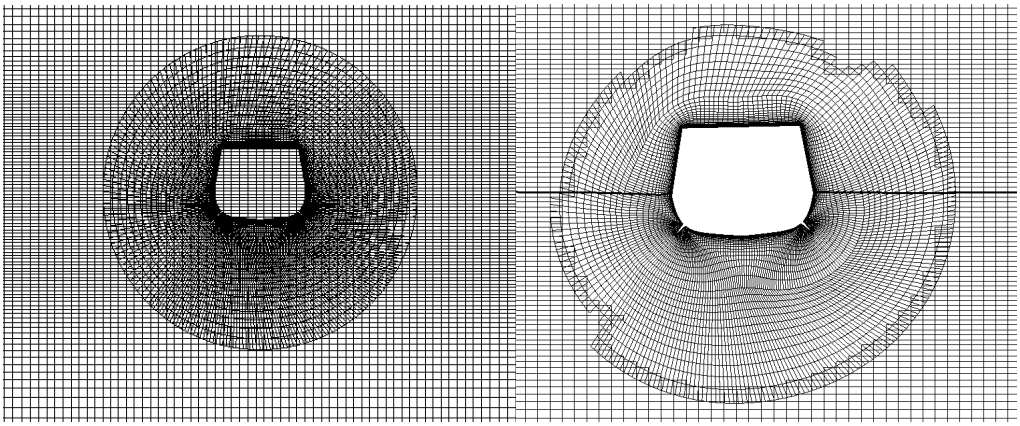

Figure 1.3: Overset grid arrangement showing hole, interpolated and active points

Carrica, *et al.* correlates ship motions using dynamic overset grids [7]. This method uses rigid overset grids that move with relative motion at large amplitude motions. The code Suggar is used to obtain interpolation coefficients between the grids at each time step that the grid is moved. This paper studied the steady-state sinkage and trim of the David Taylor Model Basin (DTMB) model 5512 advancing in calm water [7]. This geometry has been one of the benchmarks in the ship-hydrodynamics community, thus the results could be easily validated with past experiments. The overset grid comparison with experimental data for sinkage, trim, and resistance showed good comparison, proving that this meshing technique allows accurate computations of ship flows in motion.

1.4 Approach

Dynamic meshing is an important aspect of simulating and representing realistic ship motions in the ocean. OpenFOAM will be the CFD tool used to perform the simulations for this thesis. A study will be performed for basic, steady and unsteady boundary layer flows for a flat plate and ship-hull geometry. Experimental data was collected at the NSWCCD and will be used as the validation benchmark.

The goal of this thesis is to gain a better understanding of boundary layer flows in viscous fluid and use that knowledge for more challenging problems, such as large amplitude ship roll motion. A comparison of the different dynamic-mesh techniques will be performed and determined which one is best suited for ship roll motion. In order to compare these techniques, each will be tested by using an incompressible, unsteady CFD solver in OpenFOAM. The ultimate goal is to have better tools to use for computational simulations, and this thesis will help users in the future choose the best dynamic-mesh technique for their application.

1.5 Agenda

The DTMB Model #5699 tumblehome geometry will be used in this thesis, which is an extruded two-dimensional model of the mid-ship section of the ONR tumblehome, to examine alternative grid types: Laplacian mesh morphing, RBF, GGI, and overset. Each grid will be prescribed to a matrix of amplitudes and frequencies. The computations will then be compared with each other as well as with experimental work. The fluid dynamics

of rolling ship hullform sections will be examined. In particular, the vortical flow field, unsteady roll moment and side forces, as well as the ship generated wave-field will be studied.

Additionally, a study of basic, steady and unsteady boundary layer flows for a flat plate and ship-hull geometry will be conducted. Two turbulence models will be examined since it is critical to prove that the flow solvers are capable of capturing the physics of oscillating flows, boundary layers and phase lags.

This work will be achieved using the foamedOver library. The latter of which is a bridging tool that links Suggar++ and the Donor interpolation Receptor Transaction library (DiRTlib) to OpenFOAM. Suggar++ [17] obtains the overset domain connectivity information, while DiRTlib [18] simplifies the addition of an overset capability.

Chapter 2

Governing Equations

There are several significant aspects of numeral simulations that play a key role in solving complex problems. These include the governing equations, the discretization methods, the numerical grid, and the solution method to solve the system of equations. The governing equations will be discussed in this chapter which consist of conservation of mass and momentum. Unfortunately, it is unrealistic to assume that free-surface ship-hydrodynamic flow is laminar and steady. Therefore, a time-averaged approach must be applied to the Navier-Stokes equations, resulting in the Reynolds-averaged Navier-Stokes equations. Then, two turbulence models, $k - \epsilon$ and Spalart-Allmaras, will be examined to close the system of equations and solve for the unknown quantities.

2.1 Conservation of Mass

The law of conservation of mass states that the rate of increase of mass within a fixed volume must equal the rate of inflow through the boundaries, shown in equation (2.1).

$$\int_V \frac{\partial \rho}{\partial t} dV = -\int_A \rho \overrightarrow{u} \cdot d\overrightarrow{A} \tag{2.1}$$

Where $\rho\,[N/m^2]$ is the density, and $\overrightarrow{u}\,[m/s]$ is the velocity vector [14]. Gauss' theorem can be applied to the right-hand side of equation (2.1) to transform the surface integral to a volume integral which becomes equation (2.2).

$$\int_A \rho\overrightarrow{u}\cdot d\overrightarrow{A} = \int_V \nabla\cdot(\rho\overrightarrow{u})dV \tag{2.2}$$

where $\nabla\,[\frac{1}{m}]$ is defined as

$$\nabla = (\frac{\partial}{\partial x}, \frac{\partial}{\partial y}, \frac{\partial}{\partial z}) \tag{2.3}$$

Equation (2.2) combined with equation (2.1) becomes:

$$\int_V [\frac{\partial\rho}{\partial t} + \nabla\cdot(\rho\overrightarrow{u})]dV = 0 \tag{2.4}$$

The differential form of the principle of conservation of mass for a single-phase is expressed as:

$$\frac{\partial p}{\partial t} + \nabla\cdot(\rho\cdot\overrightarrow{u}) = 0 \tag{2.5}$$

For multiphase flow, another term α is introduced in the continuity equation which represents the different phases present. The Combined Phase Continuity Equation [4] is:

$$\frac{\partial}{\partial t}(\sum_N \rho_N\,\alpha_N) + \frac{\partial}{\partial x_i}(\sum_N \rho_{N_j N_i}) = 0 \tag{2.6}$$

Equation (2.6) reduces to equation (2.7), which looks similar to equation (2.5) except with the added α term.

$$\frac{\partial \rho}{\partial t} + \frac{\partial}{\partial x_i}(\sum_N \rho_N \, \alpha_N \, u_{Ni}) = 0 \tag{2.7}$$

2.2 Conservation of Momentum

The law of conservation of momentum can be expressed by applying Newton's law of motion to an infinitesimal fluid element. The net force on the element must equal mass times the acceleration of the element.

$$\rho \frac{Du_i}{Dt} = \rho g_i + \frac{\partial \tau_{ij}}{\partial x_j} \tag{2.8}$$

Equation (2.8) holds true for any continuum, solid or fluid, and the stress tensor τ_{ij} can be related to the deformation field. Equation (2.8) is known as Cauchy's equation of motion. For incompressible Newtonian fluids, the stress tensor can be expressed as equation (2.9), also known as the constitutive equation.

$$\tau_{ij} = -p\delta_{ij} + 2\mu e_{ij} \tag{2.9}$$

Where $\mu \, [Ns/m^2]$ is the dynamic viscosity, $e_{ij} \, [\frac{1}{s}]$ is the strain rate tensor and δ_{ij} is the Kronecker Delta:

$$\delta_{ij} = \begin{cases} 1 \; if \; i = j \\ \\ 0 \; if \; i \neq j \end{cases} \tag{2.10}$$

The equation of motion for a Newtonian fluid can be obtained by combining equation (2.8) and (2.9), and using vector notation, the single-phase Navier-Stokes equation reduces to:

$$\rho \frac{Du}{Dt} = -\nabla p + \rho g + \mu \nabla^2 u \tag{2.11}$$

However, when considering multiphase flow, α is added to equation (2.11) which then becomes the Combined Phase Momentum Equation [4] shown in equation (2.12).

$$\frac{\partial}{\partial t}(\sum_N \rho_N \, \alpha_N \, u_{Nk}) + \frac{\partial}{\partial x_i}(\sum_N \rho_N \, \alpha_N \, u_{Ni} \, u_{Nk}) = \rho g - \frac{\partial p}{\partial x_k} + \frac{\partial \sigma^D_{Cki}}{\partial x_i} \tag{2.12}$$

2.3 Reynolds-Averaged Navier-Stokes (RANS) Equations

The time-averaging process is applied to the conservation of mass (equation 2.5) and momentum (equation 2.11) to obtain the Reynolds-averaged equations of motion:

$$\frac{\partial U_i}{\partial x_i} = 0 \tag{2.13}$$

$$\rho\frac{\partial U_i}{\partial t} + \rho\frac{\partial u_i u_j}{\partial x_j} = -\frac{\partial P}{\partial x_i} + \frac{\partial}{\partial x_j}(2\mu S_{ij} - \overline{\rho u_j' u_i'}) \tag{2.14}$$

Equation (2.14) is the Reynolds-averaged Navier-Stokes equation, where $-\overline{\rho u_i' u_j'}$ is the Reynolds-stress tensor [28]. τ_{ij} is a symmetric tensor and has six independent components. For three-dimensional (3D) flow, there are ten unknown quantities: one pressure term, three velocity components and six Reynolds-stress components. With only four equations, we must close the system and use a turbulence model to solve for the six unknown quantities.

2.3.1 $k-\epsilon$ Turbulence Model

The most popular and widely used two-equation model is the $k-\epsilon$ turbulence model. A two-equation model means that two transported variables are solved for, that keep track of quantities such as convection and diffusion of turbulent energy in the flow. The eddy viscosity, turbulent kinetic energy, and dissipation equations are modeled to close the system of algebraic equations. Transport of momentum by turbulent eddies is modeled by an eddy viscosity, shown in equation (2.15).

$$\mu_T = 0.09\rho k^2/\epsilon \tag{2.15}$$

The turbulent kinetic energy determines the amount of energy in the turbulent flow and is characterized in equation (2.16), where σ_k= 1.0.

$$\rho\frac{\partial k}{\partial t}+\rho U_j\frac{\partial k}{\partial x_j}=\tau_{ij}\frac{\partial U_i}{\partial x_j}-\rho\epsilon+\frac{\partial}{\partial x_j}[(\mu+\mu_T/\sigma_k)\frac{\partial k}{\partial x_j}] \tag{2.16}$$

The turbulent dissipation, or ϵ, determines the length scale of the turbulent flow and is characterized in equation (2.17) , where $C_{\epsilon 1}$= 1.44, $C_{\epsilon 2}$= 1.92, σ_ϵ= 1.3.

$$\rho\frac{\partial \epsilon}{\partial t}+\rho U_j\frac{\partial \epsilon}{\partial x_j}=C_{\epsilon 1}\frac{\epsilon}{k}\tau_{ij}\frac{\partial U_i}{\partial x_j}-C_{\epsilon 2}\rho\frac{\epsilon^2}{k}+\frac{\partial}{\partial x_j}[(\mu+\mu_T/\sigma_\epsilon)\frac{\partial \epsilon}{\partial x_j}] \tag{2.17}$$

2.3.2 Spalart-Allmaras Turbulence Model

The Spalart-Allmaras (SA) model is a one-equation model, which solves a modeled transport equation for kinematic eddy viscosity [13]. The unique aspect of this model is that it is not necessary to calculate a length scale related to the local shear layer thickness. The kinematic eddy viscosity term modeled is shown in equation (2.18).

$$\nu_T=\tilde{\nu}f_{\nu 1} \tag{2.18}$$

The eddy viscosity equation is shown in equation (2.19) where $c_{b1}=0.1355$, $c_{b2}=0.622$, $\sigma=2/3$, $c_{\omega 1}=\frac{c_{b1}}{k^2}+\frac{(1+c_{b2})}{\sigma}$, $c_{\omega 2}=0.3$, $k=0.41$.

$$\frac{\partial \tilde{\nu}}{\partial t}+U_j\frac{\partial \tilde{\nu}}{\partial x_j}=c_{b1}\tilde{S}\tilde{\nu}-c_{\omega 1}f_\omega(\frac{\tilde{\nu}}{d})^2+\frac{1}{\sigma}\frac{\partial}{\partial x_k}[(\nu+\tilde{\nu})\frac{\partial \tilde{\nu}}{\partial x_k}]+\frac{c_{b2}}{\sigma}\frac{\partial \tilde{\nu}}{\partial x_k}\frac{\partial \tilde{\nu}}{\partial x_k} \tag{2.19}$$

In the eddy viscosity equation, $c_{b1}\tilde{S}\tilde{\nu}$ is the production term,$-c_{\omega 1}f_{\omega}[\frac{\tilde{\nu}}{d}]^2$ is the destruction term, and $\frac{1}{\sigma}\frac{\partial}{\partial x_k}[(\nu+\tilde{\nu})\frac{\partial \tilde{\nu}}{\partial x_k}]+\frac{c_{b2}}{\sigma}\frac{\partial \tilde{\nu}}{\partial x_k}\frac{\partial \tilde{\nu}}{\partial x_k}$ is the diffusion term.

Chapter 3

Numerical Methods

The CFD process consists of recognizing the problem statement, defining the geometry, identifying the fluid, flow, initial and boundary parameters and then generating a suitable mesh. The simulation is solved on a computer, at which time post-processing and flow visualization are performed. The mesh is refined and the process is repeated until convergence is reached. This process will be followed for the simulations completed in this thesis. In the last chapter, the governing equations were discussed but now they must be solved. This chapter will discuss the finite volume discretization method.

In order to discretize the governing equations, a suitable mesh is needed. The types of numerical grids that can be utilized include unstructured (tetrahedral, hexahedral, polyhedral) and structured. After the flow simulation is solved, there are several properties of numerical solution methods that can assist a user with determining the validity of the solution, which includes: consistency, stability, convergence, conservation and accuracy. Last, the dynamic mesh-motion techniques used in this thesis will be examined, which include Laplacian mesh morphing, RBF, GGI and overset.

3.1 Discretization

Most partial differential equations (PDE) cannot be solved analytically due to their complex structure. Approximations of the differential equations by a system of algebraic equations need to be assembled to obtain the solution, which is known as a discretization method. These algebraic equations will be used to solve for the unknown variables at a set of discrete locations in space and time. The three methods for discretizing PDE's include: finite element, finite difference and finite volume [10]. The finite volume method uses the integral form of the conservation equation and after applying the divergence theorem to volume integrals, applies an approximation to the surface integral by the midpoint rule, trapezoid rule, or Simpson's rule.

Once a discretization process is adopted, the method of approximation must be chosen. For example, in finite volume methods, one must decide on the method of approximating the surface and volume integrals. These methods could include upwind interpolation (UDS), linear interpolation (CDS), or quadratic upwind interpolation (QUICK), just to name a few. There are certain advantages to each scheme that would inherently make a user choose one scheme over another. For example, upwind interpolation is a first-order accurate method, but prevents oscillatory solutions. Linear interpolation is a second-order accurate solution, but may produce oscillatory solutions. The most important fact that needs to be considered is the type of problem being solved and the accuracy of the solution needed. If the solution does not need to be second-order accurate, a more stable first-order accurate method would be more beneficial.

3.2 Linear Equation Systems

Once a set of PDE's are discretized, a set of linear equation systems can be solved by several different methods which include direct methods (Gauss Elimination, LU Decomposition, Tridiagonal Systems), and iterative methods (Jacobi, Explicit Euler, Implicit Euler, Crank-Nicolson).

The matrix notation that represents a set of linear algebraic equations to be solved numerically is given by equation (3.1).

$$A\phi = Q \tag{3.1}$$

Gauss Elimination is the most basic method for solving systems of algebraic equations. The concept of Gauss Elimination is to create an upper triangular matrix by a method known as forward elimination. This creates a simple set of equations to be solved. However, it does not vectorize or parallelize well. LU Decomposition has been valuable to the CFD community and is a variation of Gauss Elimination. LU Decomposition uses the original matrix A, but multiplies it by a lower triangular matrix. The advantage to LU Decomposition over Gauss Elimination is that the factorization can be accomplished without any knowledge of vector Q. However, iterative methods are usually the method of choice due to the ability to solve non-linear problems. The idea of iterative methods is to create a guess for the problem and use the equations to systematically improve upon the answer. This iterative procedure creates a residual ρ^n which is represented in equation

(3.2), where ϕ^n is an approximation to the solution. The goal of iterative methods is to drive the residual value to zero.

$$A\phi^n = Q - \rho^n \tag{3.2}$$

3.3 Properties of Numerical Solution Methods

Consistency, stability, convergence, conservation, and accuracy are all crucial factors of CFD that need to be investigated before affirming that a problem is solved correctly. One error that is always present when an equation is discretized is the truncation error [10]. The truncation error is the difference between the discretized and exact equation. For a solution to be consistent, the truncation error must become zero as the grid spacing tends to zero. However, stability is also required for a system to be consistent. Stability demands that a solution does not diverge or magnify errors when using an iterative process. Certain factors that frequently help retain stability are under-relaxation values and small time step values. Similar to consistency, convergence requires that the truncation error decreases as the grid spacing goes to zero. However, convergence is checked by a series of numerical experiments. This encompasses several successively refined grids to solve for a grid-independent solution. Another relevant factor of CFD is conservation. The conservation of mass, momentum, and energy must be respected in both the local and global sense. This essentially means that the amount of quantity entering and leaving a volume at steady state without a sink or source must be equal. Finally, accuracy

is a measure of the order of approximation of the system. The order of approximation tells us the rate at which the error decreases with reduced mesh size. These errors that are referred to are the modeling errors, discretization errors, and iteration errors. All of these criteria (consistency, stability, convergence, conservation and accuracy) must be considered when examining a numerical solution.

3.4 Mesh-Motion Techniques

When choosing a type of mesh-motion technique, there are several factors that need to be considered. It is critical to preserve a high mesh quality to obtain an accurate solution. Cell skewness and non-orthogonality are two attributes that can affect the mesh quality. The computational efficiency and ease of parallel implementation are also vital when deciding upon a dynamic mesh-motion technique. The four techniques that are discussed in this section are dynamic remeshing via solution of a Laplace equation, Radial Basis Function (RBF), Generalized Grid Interface (GGI), and overset.

3.4.1 Laplacian Mesh Morphing

The mathematical representation for mesh motion via solution of a Laplace equation is shown below in equation (3.3),

$$\nabla \cdot (k \nabla u_{i,mesh}) = 0 \tag{3.3}$$

where $u_{i,mesh}$ is the velocity of points in the mesh and k, shown in equation (3.4), is a distance function that minimizes the mesh distortion, and l is the distance to the moving boundary [23].

$$k = \frac{1}{l^2} \tag{3.4}$$

The body is rotated or transformed in some manner described by the user and the points on the body are moved based on a coordinate transformation. The points surrounding the body are moved based on the Laplace equation above. There is a modest amount of error introduced before the cells surrounding the body are moved. This error describes the skewness of each cell and helps determine which cells should move. A smoothing function is introduced at this time. The domain of the problem becomes a boundary value problem to satisfy the given boundary conditions.

3.4.2 Radial Basis Function

RBF is a type of dynamic mesh technique that can support large translations and rotations by maintaining a high mesh quality during these movements. Bos [3] analyzed the RBF technique but his simulations only involved laminar flow regime with up to four processors in parallel. This thesis is interested in turbulent flow regimes and partitioning the mesh to run on more than four processors. RBF is computationally demanding, expensive, and runs much slower than other methods. The benefit of using RBF interpolation is shown by the superior mesh quality that is retained even after large rotations.

The interpolation function s(x) in equation (3.5) describes the displacement of all computational mesh points by summing a set of basis functions:

$$s(x) = \sum_{j=1}^{N_b} \Upsilon_j \phi(\parallel x - x_{b_j} \parallel) + q(x) \tag{3.5}$$

where $x_{b_j} = [x_{b_j}, y_{b_j}, z_{b_j}]$ are the boundary value displacements, q is a polynomial, N_b is the number of boundary points, ϕ is a given basis function as a function of the Euclidean distance $\parallel x \parallel$. One of the first steps in solving equation (3.5) is to evaluate the interpolation function s(x) in the known boundary points in equation (3.6).

$$s(x_{b_j}) = \triangle x_{b_j} \tag{3.6}$$

Where $\triangle x_{b_j}$ contains the known discrete values of the boundary point displacements. Once equations (3.5) and (3.6) are solved, and equation (3.7) below calculates the displacements of all internal fluid points, this information is transferred to the mesh motion solver, where the internal points are updated.

$$\triangle x_{in_j} = s(x_{in_j}) \tag{3.7}$$

By using this type of interpolation scheme, a partial differential equation is not solved and no mesh connectivity is necessary. However, there are two different avenues that can be chosen when using RBF: global or compact support. The highest mesh quality can

be obtained using global support, but requires more CPU compared to compact support. Radial Basis Functions with compact support display the criteria in equation (3.8)

$$\phi(x/r) = \begin{cases} f(x/r) & 0 \leq x \leq r, \\ 0 & x > r, \end{cases} \tag{3.8}$$

where $f(x/r) \geq 0$ is scaled with a support radius r [3]. This radius value that is chosen is significant because all of the points within the given r value are influenced by the movement of the boundary points. Larger values of r increase the accuracy of the solution but create a denser matrix system requiring more CPU. RBFs with global support compared to compact support cover the whole computational domain. There are six functions that can be used for global support, listed in Table 3.1.

RBF Name	Abbreviation	f(x)
Thin plate spline	TPS	$x^2 log(x)$
Multiquadratic Bi-harmonics	MQB	$\sqrt{a^2 + x^2}$
Inverse Multiquadratic Bi-harmonics	IMQB	$\sqrt{\frac{1}{a^2+x^2}}$
Quadratic Bi-harmonics	QB	$1 + x^2$
Inverse Quadratic Bi-harmonics	IQB	$\frac{1}{1+x^2}$
Gaussian	Gauss	e^{-x^2}

Table 3.1: Radial basis functions with global support

Considering how time-consuming RBF can be, a smoothing function has been incorporated to help increase the efficiency. The user is required to specify R_{inner} and R_{outer}

used in equation (3.9), which are the two radii of interest. The mesh is broken into three separate parts, which is specified by equation (3.10). Lastly, the evaluation function from equation (3.7) is multiplied by $\psi(\widetilde{x})$ to acquire equation (3.11), which ultimately alters the radial basis function interpolation.

$$\widetilde{x} = \frac{\parallel x_i - R_{inner} \parallel}{R_{outer} - R_{inner}} \tag{3.9}$$

$$\psi(\widetilde{x}) = \begin{cases} 1 & \widetilde{x} \leq 0 \\ 1 - \widetilde{x}^2(3 - 2\widetilde{x}) & 0 \leq \widetilde{x} \leq 1 \\ 0 & \widetilde{x} \geq 1 \end{cases} \tag{3.10}$$

$$\triangle\widetilde{x}_{inj} = s(x_{inj}) \cdot \psi(\widetilde{x}) \tag{3.11}$$

The smoothing function does not alter the RBF interpolation within R_{inner}, as $\psi(\widetilde{x}) = 1$, because equation (3.11) becomes equation (3.7) and the RBF interpolation behaves as expected. However, when $\widetilde{x}$ is between zero and one, the smoothing function increases in strength as $\widetilde{x}$ goes from zero to one. When $\widetilde{x}$ is greater than or equal to one, the points in the system become fixed and no interpolation occurs. These points are not involved in the moving boundary because the value of the RBF becomes zero, and these points are neglected.

3.4.3 Generalized Grid Interface

GGI has been used primarily in the turbomachinery industry due to the large rotations of rotor blades. GGI allows for one patch to remain stationary while a connected patch moves without a complicated interpolation algorithm between the two. This makes GGI relatively robust. The most time-consuming aspect of using GGI comes from the mesh generation. At the interface of the stationary and rotating patches, there must exist two submeshes. These patches can not overlap but should be as close as possible to avoid inaccuracies due to gaps. The only specified information needed by OpenFOAM is the two clearly defined patches (stationary and moving), a point inside the moving mesh and a point and axis of rotation.

There are few equations that are associated with the GGI method. The finite volume discretization on a GGI interface can be displayed as a sum of facet operations, shown in equation (3.12).

$$\phi_N^s = \sum_t W_t \phi_t \tag{3.12}$$

ϕ_N^s represents the shadow neighbor values for the front of the face, while t denotes the values on the other side of the face [2]. This concept can be more easily understood by breaking up ϕ_N^s into the master patch and shadow patch for a mesh, shown in equations (3.13) and (3.14),

$$\phi_{Si} = \sum_{n} W_{M_n toS_i} * \phi_{M_n} \tag{3.13}$$

$$\phi_{Mj} = \sum_{m} W_{S_m toM_j} * \phi_{S_m} \tag{3.14}$$

where ϕ_S is a shadow patch variable, ϕ_M is the master patch variable, W_{MtoS} is the master facet to shadow facets weighting factor, W_{StoM} is the shadow facet to master facets weighting factor, n is the number of master facet neighbors for shadow patch i, and m is the number of shadow facet neighbors for master patch j. Equation (3.15) displays the constraint for this discretization method, which states that it must be conservative for all faces on both sides of the interface.

$$\sum_{t} W_t = 1 \tag{3.15}$$

After the GGI interface is discretized properly, an interpolation scheme must be used. The general form used for interpolation for the master and shadow patches is shown below in equation (3.16).

$$W_t = \frac{S_{facet}}{S} \tag{3.16}$$

W_t is the GGI weighting factor which can be calculated from the surface intersection area between the two patches (S_{facet}) and the surface area of the master of shadow patch (S).

3.4.4 Overset Methods

The overset method reduces a single, complex domain into component meshes. This can be advantageous for several reasons. First, the grid can be broken into parts in which different people can work together to construct different parts of the domain. If a grid is broken into several blocks, small modifications can be made to component blocks and the entire grid system does not have to be re-meshed. Also, design variances can be explored easily with overset grids as well as piecewise build up of complex configurations.

The domain for overset methods is broken into two sections: static and moving grids. As implied, the static grids do not move and are the fixed reference frame responsible for resolving the free surface. The far field boundary conditions are specified on the static grids. The moving grid is attached to the moving body in the domain and is fully engrossed in the static grid [7]. There are three types of grid points that are recognized in the overset approach: active, interpolated or hole. Active points can be from the static or moving grids and store information about the solution. Hole points are located on a body or outside the computational domain and therefore are excluded from the solution. Interpolation points are located between the hole and active points and overlap the static grid. Information is interpolated between the two grids at each time step by interpolation coefficients shown in equation (3.17).

$$\varphi_{int} = \sum_{d=1}^{8} a_d \varphi_d \tag{3.17}$$

The Suggar code developed by Ralph Noack is responsible for the overset domain connectivity between the static and moving grids [16]. If the number of cells in a computation is less than a million, the amount of CPU time that Suggar takes is less than 5% [16]. Suggar is a separate process from the flow solver but both work in tandem to move the mesh, reduce the amount of overlap between the grids, and solve for the unknown variables. This process is displayed in Figure 3.1.

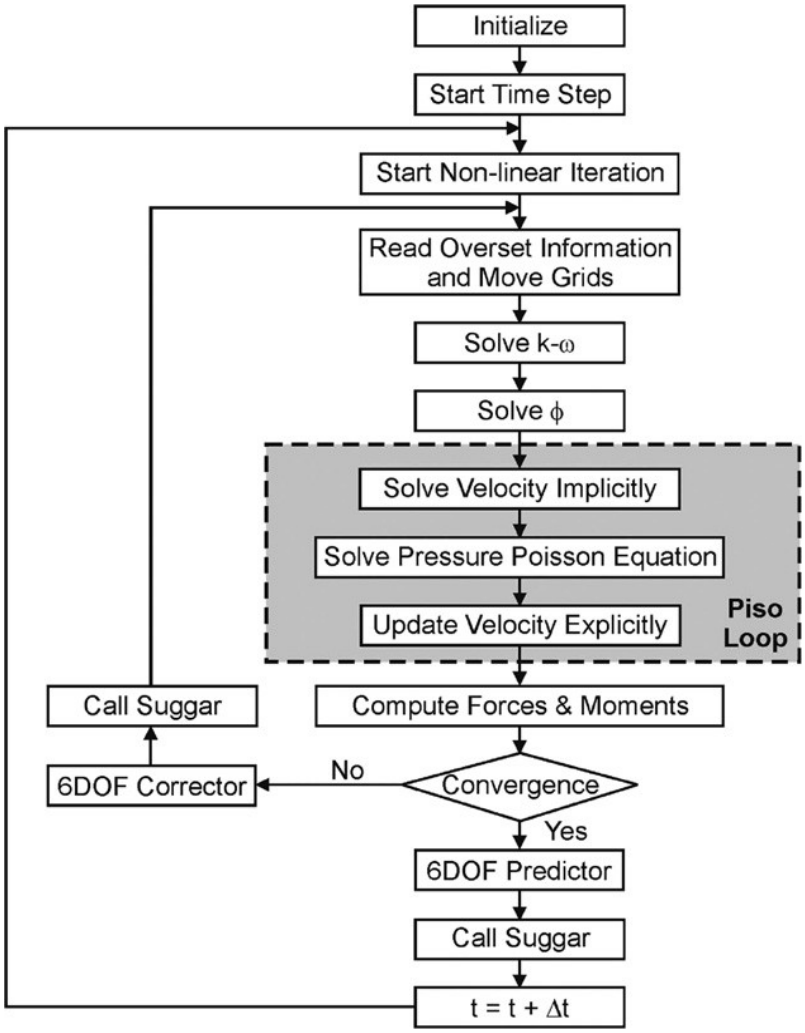

Figure 3.1: Overset Procedure

Chapter 4

Flat Plate Boundary Layer Flows

Unsteady boundary layer flows over ships is of particular importance when studying ship-hydrodynamics. Therefore, this chapter is intended to set the frame-work for understanding viscous dominated flows. This chapter will study basic, steady and unsteady boundary layer flows for a flat plate geometry. Additionally, it is critical to prove that the flow solvers are capable of capturing the physics of oscillating flows, boundary layers and phase lags. First, a steady boundary layer on a flat plate is examined, using the Spalart-Allmaras (SA) and $k-\epsilon$ turbulence models. Next, an unsteady boundary layer on an oscillatory flat plate is studied. This replicates the analytic solution of Stokes second problem [14]. Here, the unsteady parallel flow does not have a similarity solution because of the natural time scale that exists. The next computation considered is an unsteady boundary layer on a flat plate due to oscillatory free-stream flow. This case is beneficial in studying phase lags, velocity overshoot in the boundary layer and examining the similarity with the Blasius solution.

4.1 Steady Boundary Layer on a Flat Plate

4.1.1 Mesh Generation

Naval experiments are conducted at two scales: model and full-scale. This section will calculate and then simulate the Reynolds numbers foreseen by model and full-scale free-surface ships. The model-scale ship that will be simulated in this chapter is the surface ship model 5415, shown in Figure 4.1. "Model 5415 is a towing tank model representing a modern naval combatant" [6].

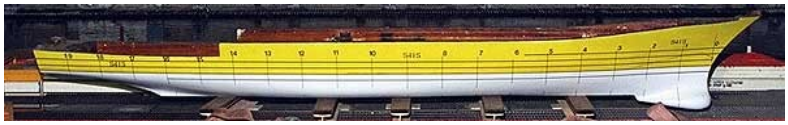

Figure 4.1: Surface Ship Model 5415

The full-scale ship denoted is the USS Arleigh Burke DDG-51, shown in Figure 4.2. "The DDG-51 is the lead ship of the Arleigh Burke-class of guided missile destroyers" [5].

Figure 4.2: USS Arleigh Burke DDG-51

These ships operate at very different Reynolds numbers, which are calculated and shown in Table 4.1. As a reminder, the Reynolds number is a dimensionless number that describes a ratio of inertial to viscous forces. It is useful to distinguish between different flow regimes such as laminar or turbulent and is characterized in equation (4.1).

$$Re = \frac{V \cdot L}{\nu} \tag{4.1}$$

Scale	Model-5415	Full-DDG51
Length (m)	5.72	153.924
Velocity (m/s)	2.0578	10.2889
Viscosity (m^2/s)	$1 \cdot 10^{-6}$	$1 \cdot 10^{-6}$
Reynolds Number	$O(10^7)$	$O\ (10^9)$

Table 4.1: Reynolds number calculations for model and full-scale ships

When the boundary layer is examined, quantities that are significant in the near-wall region need to be employed [26]. Before nondimensional variables can be used, a friction velocity that has constant properties in the boundary layer must be defined, shown in equation (4.2).

$$u_\tau = \sqrt{\tau_o/\rho} \tag{4.2}$$

The friction velocity can directly be used to define a nondimensional velocity (equation 4.3) and nondimensional length (equation 4.4) that is advantageous in regards to describing the boundary layer.

$$u^+ = \frac{\bar{u}}{u_\tau} \tag{4.3}$$

$$y^+ = \frac{y \cdot u_\tau}{\nu} \tag{4.4}$$

The boundary layer is separated into three distinct regions when considering Couette flow: the viscous sublayer characterized in equation (4.5), the buffer layer and the logarithmic region shown in equation (4.6).

$$u^+ = y^+ \tag{4.5}$$

$$u^+ = \frac{1}{k} \ln y^+ + \beta \qquad y^+ \leq 10^9 \tag{4.6}$$

The Spalart-Allmaras and $k - \epsilon$ turbulence models will be used for the CFD simulations in this section. The SA model was simulated with y^+ values of one and one hundred,

the later of which will need wall functions to resolve the viscous sublayer. A y^+ value of one was chosen so there would be grid points present where the largest velocity gradients occur, i.e. viscous sublayer. Also, it is understood that at y^+ of one hundred the grid points would be in the log-layer, which is required to use wall functions with most flow solvers. The $k-\epsilon$ model requires wall functions since the mesh was generated with a y^+ value of one hundred. The Reynolds numbers for the 5415 and DDG-51 ships can now be used in equation (4.7) to calculate the near-wall spacing that is needed for a desired y^+ value.

$$\triangle y = \frac{y^+}{\sqrt{2 \cdot C} \cdot Re_L} \tag{4.7}$$

Four meshes were generated using a flat plate geometry with calculated $\triangle y$ values given in Table 4.2. All four grids are analogous, therefore only one is displayed in Figure 4.3.

	$\triangle y$	y^+	Re_L
Grid 1	$2.7 \cdot 10^{-6}$	1	10^7
Grid 2	$4.3 \cdot 10^{-8}$	1	10^9
Grid 3	$2.7 \cdot 10^{-4}$	100	10^7
Grid 4	$4.3 \cdot 10^{-6}$	100	10^9

Table 4.2: Near-wall spacing calculations

The near-wall spacing calculations from Table 4.2 were used in constructing the grid shown in Figure 4.3. This grid was generated with structured cells using the program Pointwise.

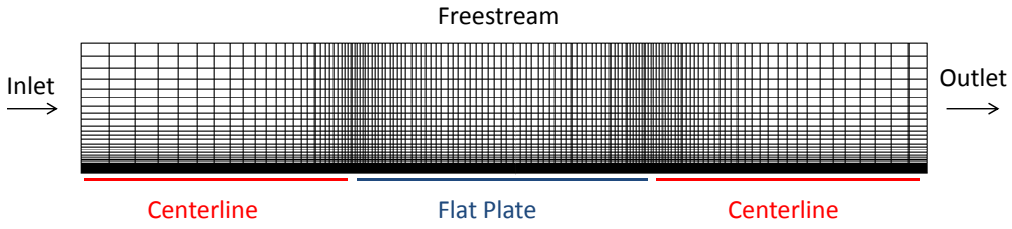

Figure 4.3: Flat Plate Grid for Steady Boundary Layer Cases

4.1.2 Boundary Conditions

The boundary conditions used in these computations are shown in Table 4.3.

Boundary	Pressure	Velocity
Inlet	ZeroGradient	FixedValue 10 m/s
Outlet	FixedValue 0	ZeroGradient
Freestream	ZeroGradient	FixedValue 10 m/s
FrontAndBack	Empty	Empty
Flat Plate	ZeroGradient	FixedValue 0
Centerline	SymmetryPlane	SymmetryPlane

Table 4.3: Boundary Conditions for Steady Boundary Layer Cases

4.1.3 Fluid Parameters

The fluid parameters used with the four grids generated are shown in Table 4.4. The grid numbers correspond to the grid numbers in Table 4.2.

Grid	1	2	3	4
Velocity (m/s)	10	10	10	10
Viscosity (m^2/s)	$1 \cdot 10^{-6}$	$1 \cdot 10^{-8}$	$1 \cdot 10^{-6}$	$1 \cdot 10^{-8}$
Density (kg/m^3)	1	1	1	1

Table 4.4: Fluid Parameters for Steady Boundary Layer Cases

4.1.4 Results

The classic turbulent boundary layer is analyzed in OpenFOAM. The boundary layer profile in wall-coordinates as well as the local wall shear stress is plotted. The model 5415 Reynolds number of 10^7 is used to create Figures 4.4 and 4.5, while the DDG51 Reynolds number of 10^9 is used in Figures 4.6 and 4.7. The law of the wall correlation and White's correlation [27] are used to compare against the computational results. The k-ϵ turbulence model and the SA turbulence model both show good correlation with the expected results. The SA model is more versatile since it can run with and without wall functions, indicating a y^+ value of one hundred and one respectively. From here after, the SA model will be used to model turbulent flow for all the following computations.

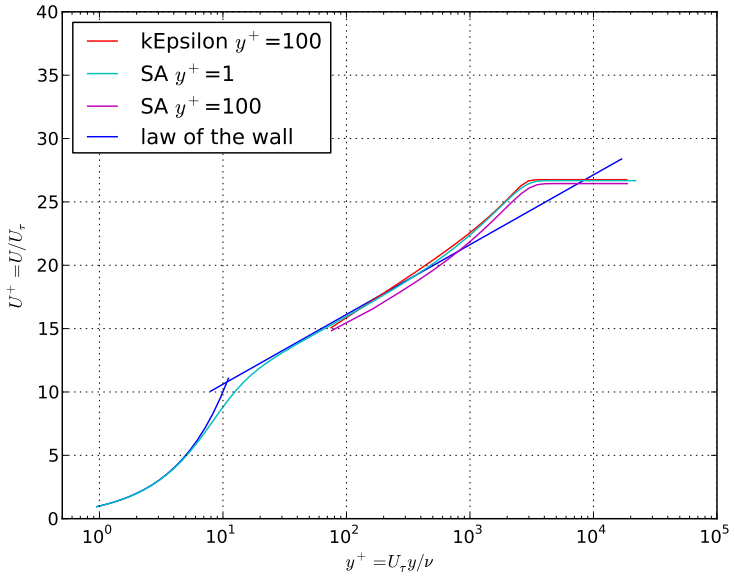

Figure 4.4: Velocity Profile in Wall Coordinates for Re_x = 10M

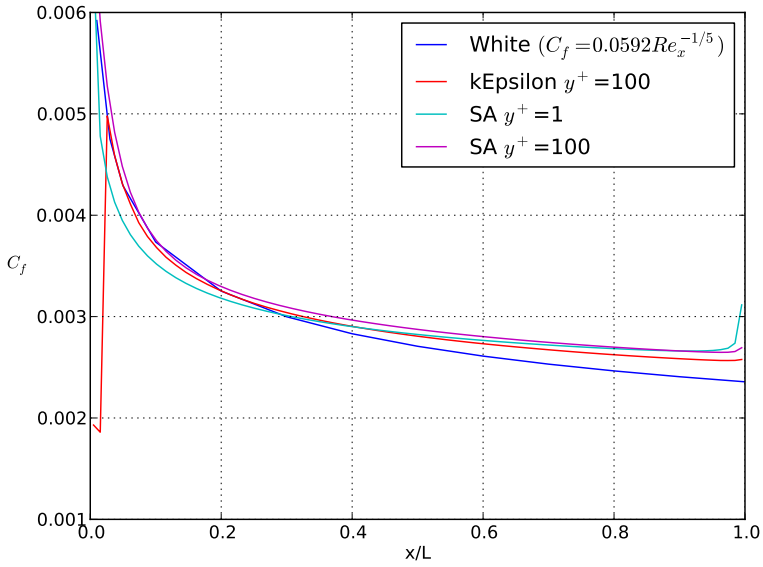

Figure 4.5: Cf vs X at Re_x = 10M

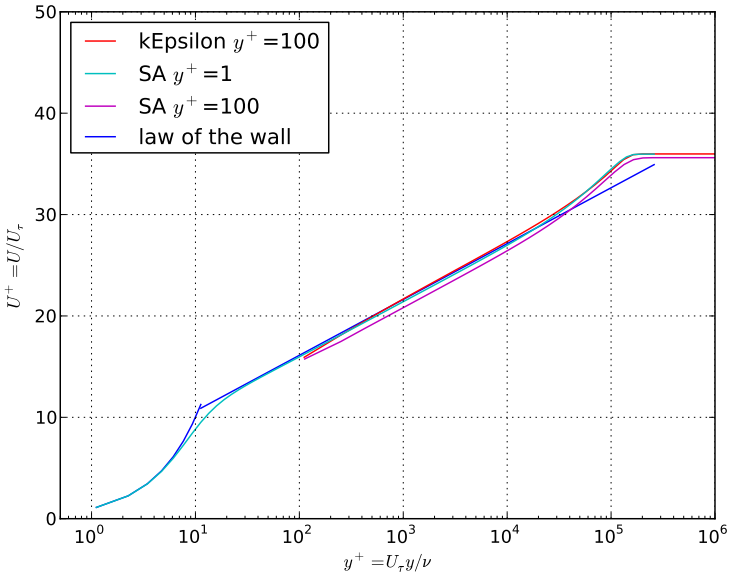

Figure 4.6: Velocity Profile in Wall Coordinates for $Re_x = 1000\text{M}$

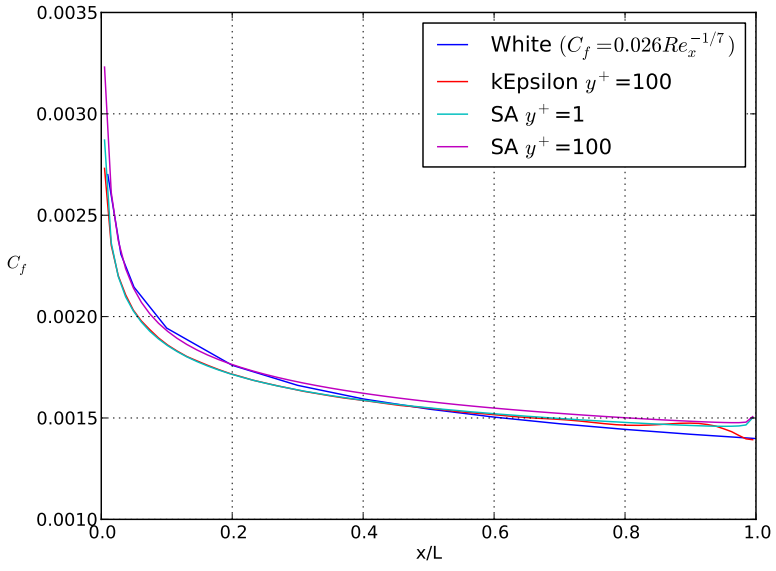

Figure 4.7: Cf vs X at $Re_x = 1000\text{M}$

4.2 Unsteady Boundary Layer on an Oscillatory Flat Plate

The sinusoidal oscillation of a flat plate, which induces motion of a viscous fluid, is known as Stokes second problem [14]. The study of this motion is useful for practical applications such as acoustic streaming around an oscillating body. Also, the oscillation of a flat plate relates to the rolling motion of a ship if it were to lay flat. The rolling motion of a ship is the ultimate study of this thesis; therefore, the concepts learned in this section are relevant to later chapters.

The sinusoidal oscillation of a flat plate is an unsteady problem, but the steady periodic solution will be analyzed. The governing equation that represents this flow is shown in equation (4.8),

$$\frac{\partial u}{\partial t} = \nu \frac{\partial^2 u}{\partial y^2} \tag{4.8}$$

which has boundary conditions of:

$$u(0,t) = U \cdot cos(\omega t)$$

$$u(\infty,t) = bounded$$

The velocity distribution of laminar flow for Stokes problem [14] is represented by the analytic solution in equation (4.9).

$$u = U \cdot e^{-y\sqrt{\omega/(2\cdot\nu)}} cos(\omega t - y\sqrt{\frac{\omega}{2\cdot\nu}}) \tag{4.9}$$

4.2.1 Mesh Generation

The mesh generation for this section was far less complicated than in section 4.1.1. Only one mesh was created to simulate Stokes second problem and is shown below in Figure 4.8. This flow was laminar, therefore turbulence models were not used and y^+ spacing near the wall was not pertinent. However, the grid spacing was created to be fine near the wall to capture the large velocity gradients due to the presence of the flat plate.

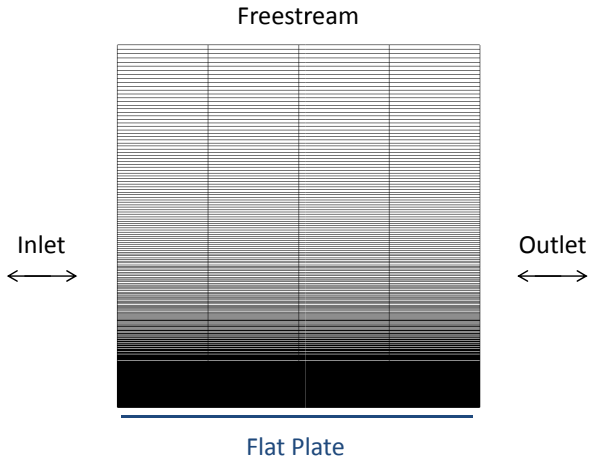

Figure 4.8: Oscillatory Flat Plate Grid

4.2.2 Boundary Conditions

The boundary conditions for this simulation are listed in Table 4.5.

Boundary	Pressure	Velocity
Inlet/Outlet	Cyclic	Cyclic
Freestream	FixedValue 0	Zero Gradient
FrontAndBack	Empty	Empty
Flat Plate	Zero Gradient	Prescribed Oscillation

Table 4.5: Boundary Conditions for the Oscillatory Flat Plate

The prescribed oscillation of the flat plate is shown below in equation (4.10):

$$A \cdot sin(\omega t) \tag{4.10}$$

where A= 0.5, and ω=10 Hz.

4.2.3 Fluid Parameters

The fluid parameters used for this grid are shown in Table 4.6.

Viscosity (m^2/s)	$1 \cdot 10^{-6}$
Density (kg/m^3)	1

Table 4.6: Fluid Parameters for the Oscillatory Flat Plate

4.2.4 Results

Stokes second problem was simulated using OpenFOAM. The profiles that are analyzed are taken at mid-plate. The velocity distributions of the analytic solution and the computational results are compared at $\omega t = 0$, $\pi/2$, π, and $3\pi/2$, shown in Figure 4.9. The analytic and computational results match very closely at all time steps. From this figure, OpenFOAM proves successful in capturing the correct velocity distribution of an oscillating flow in laminar conditions with zero mean flow.

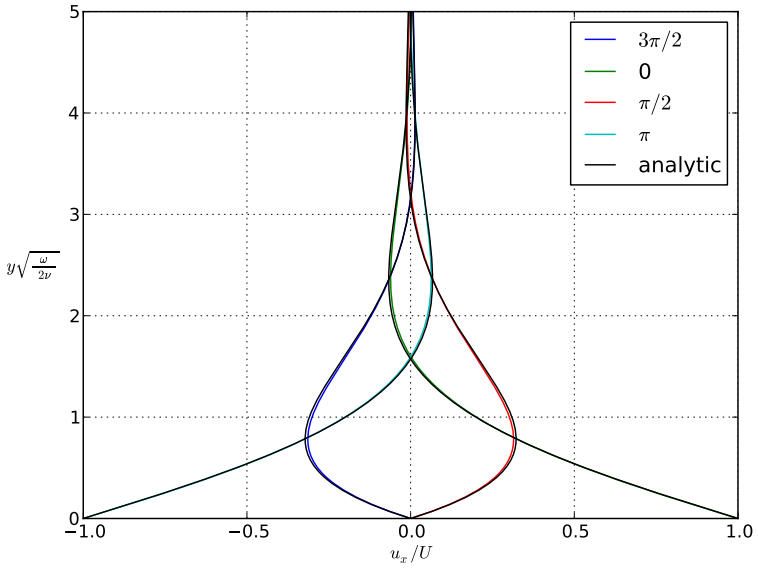

Figure 4.9: Stokes second problem, analytic vs computational results

4.3 Unsteady Boundary Layer on a Flat Plate Due to Oscillatory Free-Stream Flow

4.3.1 Mesh Generation

A computational study was conducted on a stationary flat plate with an oscillating, non-zero mean flow, which creates an unsteady boundary layer. The geometry used for this simulation is the same as the previously generated mesh, shown in Figure 4.3 for reference.

4.3.2 Boundary Conditions

However, the boundary conditions for this section are different than those in section 4.1. The freestream and inlet values are prescribed to an oscillation, defined by equation (4.11):

$$U_e(t) = U_0 + U_1 sin(\omega t) \tag{4.11}$$

where U_e is the external-flow velocity, U_0 is the uniform-stream velocity, U_1 is the unsteady velocity amplitude, and ω is the dimensional frequency [24]. The input values for equation (4.11) were chosen by replicating an experiment by Choi, who studied temporal, spatial, and traveling waves [8]. Choi simulates the temporal wave by using a Reynolds number of 10^4, a value of U_1 to be $0.4 \cdot U_0$, and lists several frequencies (ξ) that he tests. This section implements values of $U_0 = 0.01$ m/s, $U_1 = 0.004$ m/s and $\omega = 0.0147$ rad/s.

All of the boundary conditions for this section are displayed in Table 4.7.

Boundary	Pressure	Velocity
Inlet	ZeroGradient	Prescribed Oscillation
Outlet	ZeroGradient	ZeroGradient
Freestream	ZeroGradient	Prescribed Oscillation
FrontAndBack	Empty	Empty
Flat Plate	ZeroGradient	FixedValue 0
Centerline	SymmetryPlane	SymmetryPlane

Table 4.7: Boundary Conditions for Oscillatory Free-Stream Flow

4.3.3 Fluid Parameters

The fluid parameters used for this grid are shown in Table 4.8.

Viscosity (m^2/s)	$1 \cdot 10^{-6}$
Density (kg/m^3)	1

Table 4.8: Fluid Parameters for Oscillatory Free-Stream Flow

4.3.4 Results

The flow physics expected from this simulation include phase lags and overshoots in the boundary layer. From Figure 4.10, the phase lags are very apparent. This figure has divided the period (T) into four parts: 0T, 0.25T, 0.5T and 0.75T. At the beginning and

middle of the period, 0T and 0.5T respectively, it is shown that the velocity approaches U_0 (0.01 m/s) in the freestream when the unsteady term approaches zero. At 0.25T, the unsteady velocity is at a maximum and increases the overall velocity in the flow. On the contrary, at 0.75T, the unsteady velocity is at a minimum and decreases the overall velocity in the freestream. This variation of instantaneous velocity is referred to as phase lags.

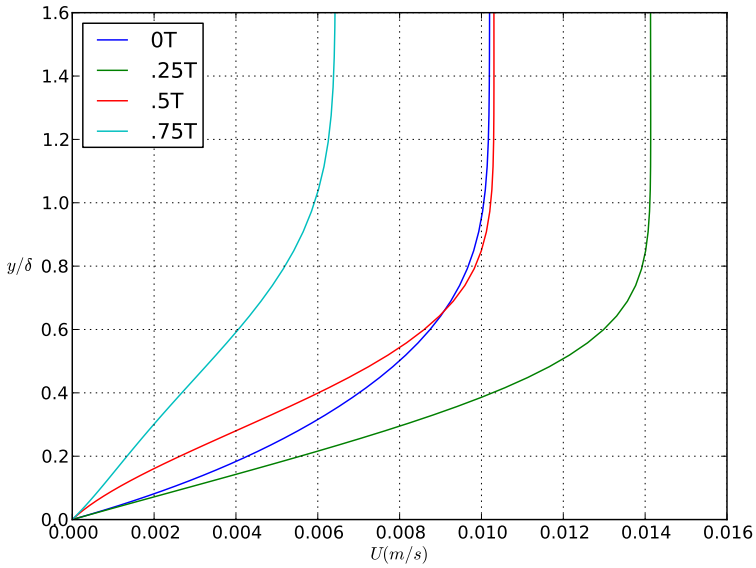

Figure 4.10: Instantaneous Velocity Observed Over One Time Period (T)

The Blasius Solution is defined as a steady two-dimensional boundary layer with constant, uniform, laminar flow parallel to a semi-infinite flat plate. This is a self-similar solution

and can therefore be compared to the CFD simulation from this section, shown in Figure 4.11. The U_{mean} value in the CFD simulation matches in good agreement with the well known Blasius Solution. However, there is a slight deviation between the two lines, which could be from the nonlinear streaming in the CFD simulation.

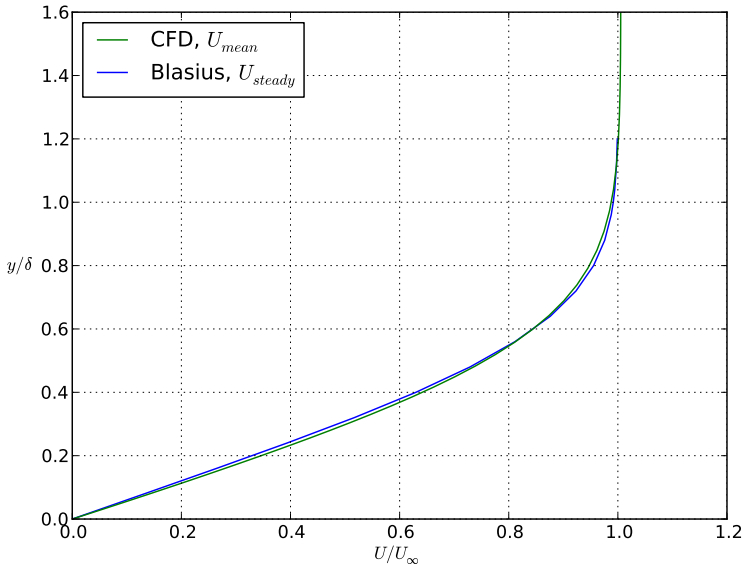

Figure 4.11: Blasius Solution vs. Mean Velocity of the CFD Simulation

This type of flow is characterized by small-amplitude overshoots that occur in the boundary layer. Figure 4.12 clearly shows that the velocity overshoots past the predicted maximum unsteady component in the boundary layer. In the freestream, however, the

unsteady component returns to the expected value of 0.004 m/s, which is the value of U_1.

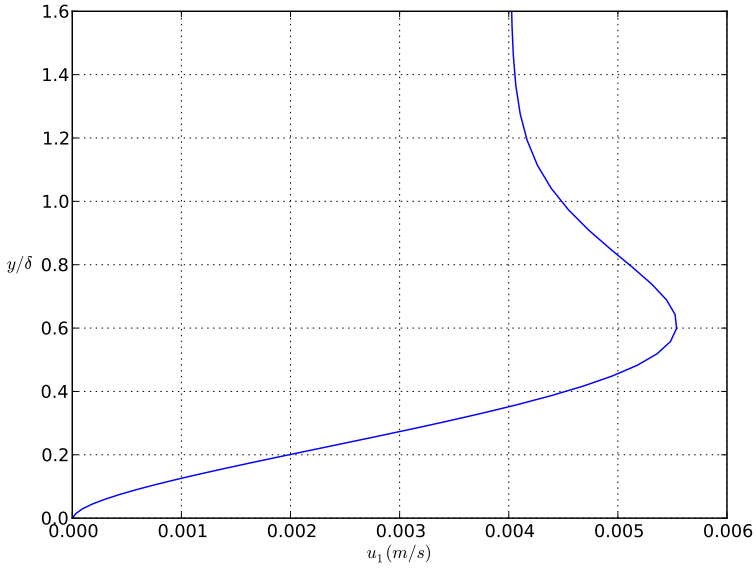

Figure 4.12: Unsteady Velocity Component in Oscillatory Free-Stream Flow Case

Chapter 5

Keulegan-Carpenter Flow

Unsteady boundary layers over ship-hull sections due to oscillatory free-stream flow will be studied in this chapter. This type of flow is known as Keulegan-Carpenter flow. The flat plate geometry studied in the last chapter was helpful for understanding basic concepts, however, it is not realistic for ship-hydrodynamics applications. This chapter will give better insight into oscillatory boundary layer flows for model-scale and full-scale ships.

5.1 Mesh Generation

The ONR tumblehome hullform with 1.25 meter bilge keel geometry will be used in this section. Figure 5.1 represents the mesh generated in Pointwise using structured-Cartesian cells.

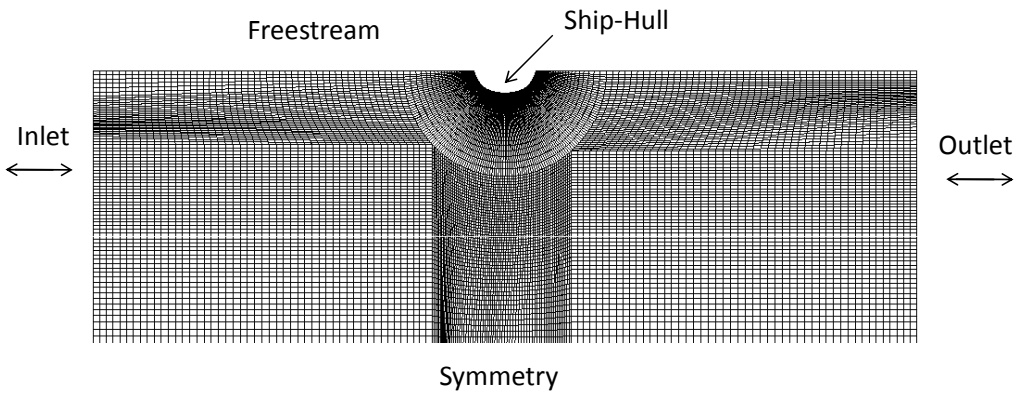

Figure 5.1: Ship-Hull Sections Grid

In the center of the grid, there is a label for ship-hull. For this part of the grid, there will be three different two-dimensional slices taken along the ONR tumblehome that will be studied. Each section represents significantly different aspects of the geometry and zoomed-in images of the sections include: barehull (Figure 5.2), bilge keels (Figure 5.3), and rudders (Figure 5.4). The grid generation process was much more complicated for ship-hull sections compared to the flat plate geometry due to the presence of bilge keels and rudders.

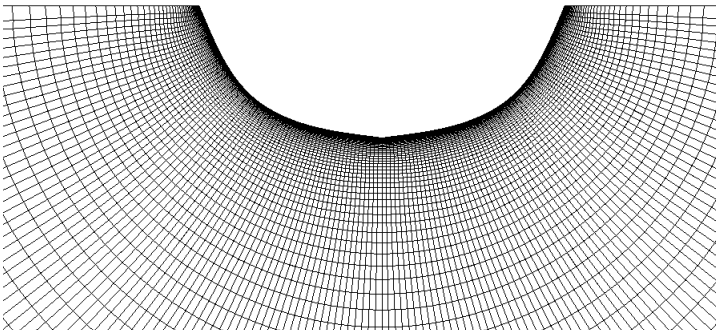

Figure 5.2: Tumblehome Barehull Grid

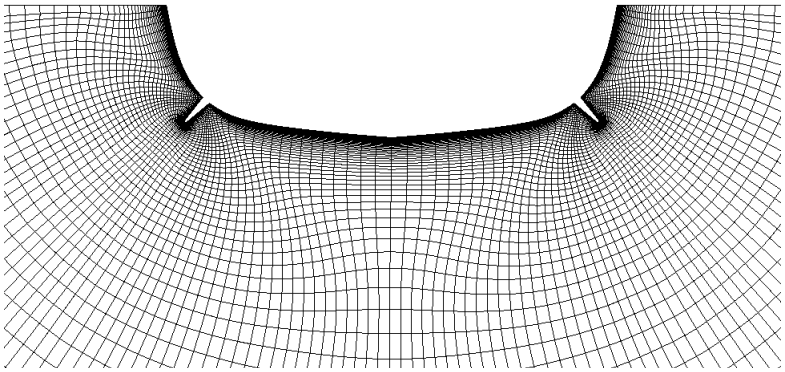

Figure 5.3: Tumblehome Bilge keel Grid

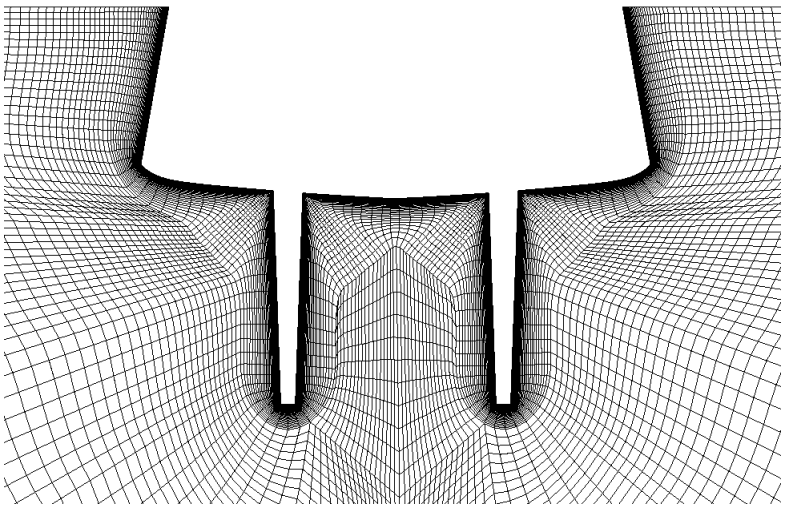

Figure 5.4: Tumblehome Rudder Grid

5.2 Boundary Conditions

The boundary conditions are the same for each ship-hull section and are listed in Table 5.1.

Boundary	Pressure	Velocity
Inlet	ZeroGradient	Prescribed Oscillation
Outlet	ZeroGradient	Prescribed Oscillation
Freestream	Total Pressure	Slip
FrontAndBack	Empty	Empty
Ship-Hull	ZeroGradient	Fixed-Value 0
Symmetry	SymmetryPlane	SymmetryPlane

Table 5.1: Boundary Conditions for Unsteady Flow around Ship-Hull Sections

The freestream and inlet values are prescribed to an oscillation, defined by equation (5.1):

$$U = U_m cos\theta \tag{5.1}$$

with $\theta = \omega t$. The value of ω was chosen to be 2.5 rad/s to match one of Bassler's experiments [1]. The meshes for this section are generated for model and full-scale parameters. The U_m value for equation (5.1) is determined by selecting a Keulegan-Carpenter number and using equation (5.2) to solve for U_m. As a reference, the Keulegan-Carpenter number is a dimensionless quantity that is related to the oscillation frequency of unsteady flow. It is a ratio of the drag forces to the inertial forces in oscillatory flow for blunt objects, shown in equation (5.2).

$$K = \frac{U_m \cdot T}{D} \tag{5.2}$$

U_m is the maximum velocity of the flow, T is the period of wave motion and D is the cylinder diameter. Another important parameter when discussing the Keulegan-Carpenter number is β, which is defined in equation (5.3).

$$\beta = \frac{D^2}{\nu \cdot T} \tag{5.3}$$

These two parameters are important when discussing the Morison Equation [21], shown in equation (5.4), representing the in-line force acting on a cylinder by a linear sum of the drag and inertial forces per unit length.

$$F = \frac{1}{2}\rho D C_d |U|U + \frac{1}{4}\pi\rho D^2 C_m \frac{dU}{dt} \tag{5.4}$$

D is the diameter of the circular cylinder, U is the velocity of the ambient flow ($U = U_m cos\theta$ with $\theta = \frac{2\pi t}{T}$), T is the period of flow oscillation, t is the time, C_d is a drag coefficient, and C_m is the inertia coefficient, the latter two determined experimentally.

5.3 Fluid Parameters

The fluid parameters used for cases in this section are shown in Table 5.2.

Viscosity (m^2/s)	$1 \cdot 10^{-6}$
Density (kg/m^3)	1

Table 5.2: Fluid Parameters for Unsteady Flow around Ship-Hull Sections

The model and full-scale grids have much different flow parameters from each other. In Table 5.3, the draft, β and period are listed for the different ship-hull sections for model-scale geometry. Table 5.4 displays the values of U_m calculated based on chosen Keulegan-Carpenter numbers. In Table 5.5, the draft, β and period are listed for the different ship-hull sections for full-scale geometry. Table 5.6 displays the values of U_m calculated based on chosen Keulegan-Carpenter numbers.

Section	Draft (m)	β	Period (s)
Midship/Forebody	0.172	11,789.5	2.51
Rudder	0.356	50,492.4	2.51

Table 5.3: Model-Scale Parameters

Section	K	U_m (m/s)	Re #
Midship/Forebody	0.4	0.0274	4714.6
Midship/Forebody	1.0	0.0685	11,786.9
Midship/Forebody	2.0	0.1371	23,572.9
Midship/Forebody	10.0	0.6853	117,865
Rudder	0.4	0.0567	20,197
Rudder	1.0	0.1418	50,492.4
Rudder	2.0	0.2837	100,985
Rudder	10.0	1.418	504,924

Table 5.4: Model-Scale Reynolds numbers for KC values

Section	Draft (m)	β	Period (s)
Midship/Forebody	5.504	$1.2 \cdot 10^7$	2.51
Rudder	11.4	$5.17 \cdot 10^7$	2.51

Table 5.5: Full-Scale Parameters

Section	K	U_m (m/s)	Re #
Midship/Forebody	0.4	0.877	$5.02 \cdot 10^6$
Midship/Forebody	1.0	2.19	$1.2 \cdot 10^7$
Midship/Forebody	2.0	4.538	$2.51 \cdot 10^7$
Midship/Forebody	10.0	21.93	$1.21 \cdot 10^8$
Rudder	0.4	1.8167	$2.07 \cdot 10^7$
Rudder	1.0	4.54	$5.18 \cdot 10^7$
Rudder	2.0	9.08	$1.04 \cdot 10^8$
Rudder	10.0	45.4	$5.18 \cdot 10^8$

Table 5.6: Full-Scale Reynolds numbers for KC values

5.4 Results

As discussed in section 5.0.6, the Morison Equation formulates the force acting on a body due to drag and inertial components. The first step in analyzing the results of this section was to determine if there was in fact both components creating the forces acting on the ship-hull sections. Figure 5.5 represents a force plot for the full-scale ship-hull sections. The blue line (case 4) clearly shows that there is a dominant component constituting the force but the other component has a smaller contribution, which can be seen through the uneven peaks of the blue line. Table 5.7 gives reference parameters for the cases specified in Figure 5.5.

The first harmonics in the Fourier Series of the F_x were computed, where a_1 represents the drag component (equation 5.5) and b_1 represents the inertial component (equation 5.6).

$$a_1 = \frac{1}{2}\rho D C_d U_m^2 \tag{5.5}$$

$$b_1 = -\frac{1}{4}\pi\rho D^2 C_m U_m \omega \tag{5.6}$$

case	Section	K	U_m (m/s)
1	Midship	0.4	0.877
2	Midship	1.0	2.19
3	Midship	2.0	4.538
4	Midship	10.0	21.93

Table 5.7: Specification of case numbers for Force Plot

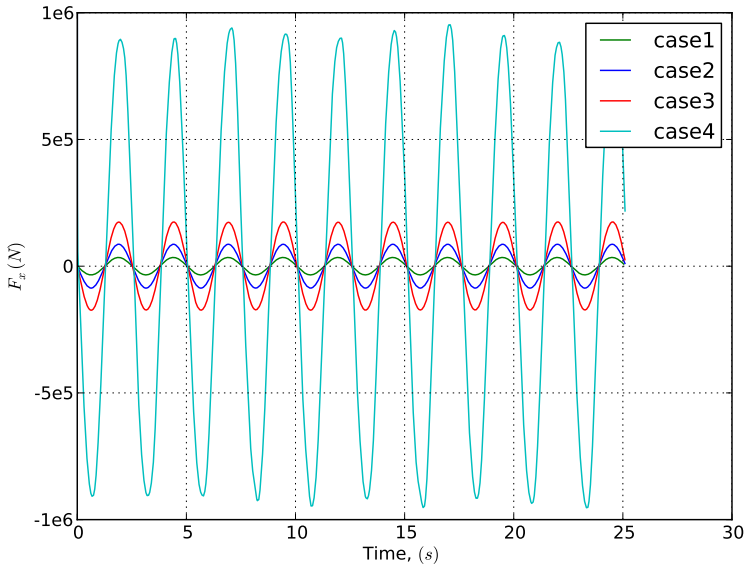

Figure 5.5: Full-Scale F_x vs Time Plot, showing that both drag and inertial components are present

A ratio of the Fourier coefficients are plotted vs K in Figure 5.6. The full-scale and model-scale lines collapse on each other for both the midship and forebody sections. The midship section has bilge keels while the forebody is a barehull section. This means that the introduction of bilge keels causes the force due to drag compared to inertia to

increase with an accelerated flow. The forebody section conserves a constant ratio of drag to inertia at every K value tested.

The trends observed for the actual drag to inertia coefficients shown in Figure 5.7 are similar for the midship and forebody sections. Again, the model-scale and full-scale lines collapse on each other for each section but the ratio of drag to inertia decreases as the value of K increases. This means that the inertia force is becoming more dominant as the flow increases.

There are no results shown for the rudder section tests because the solutions are not converging. A further spacial and time study would need to be completed to acquire a converged solution. The extremely large rudders that protrude in the water make it very difficult to obtain a highly resolved mesh.

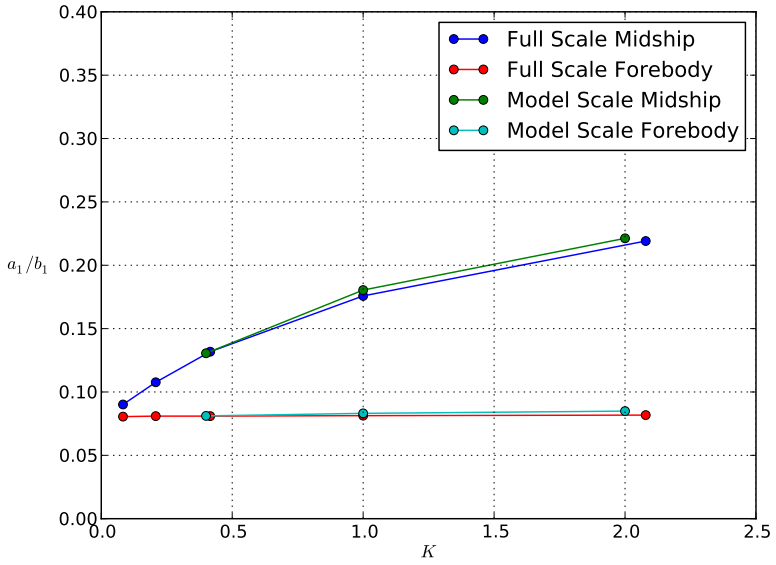

Figure 5.6: Ratio of Fourier Coefficients vs K

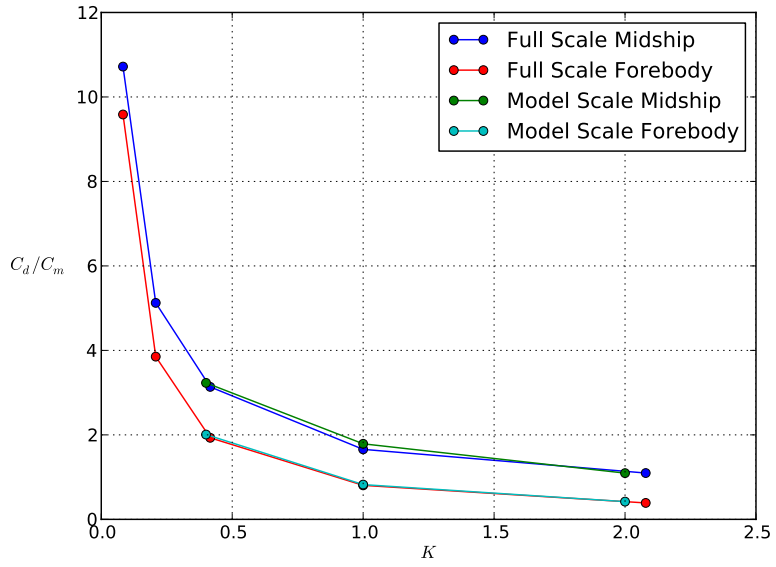

Figure 5.7: Ratio of Drag Coefficient to Inertia Coefficient vs K

Chapter 6

Unsteady Boundary Layer Flows due to Roll Motion

This chapter presents the dynamic-mesh techniques for unsteady surface-ship hydrodynamics. The ONR tumblehome will be used as the surface-ship for these calculations. The four types of dynamic-mesh techniques studied are Laplacian mesh motion, RBF, GGI, and overset. For each case, the grid, simulation parameters, and analysis is presented.

6.1 Mesh Generation

The ONR tumblehome mid-ship section that will be analyzed in this chapter is shown in Figure 6.1.

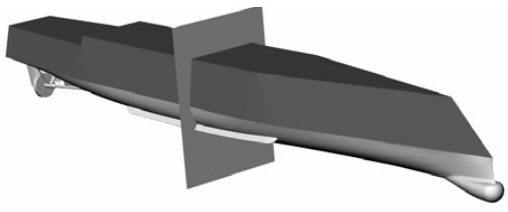

Figure 6.1: ONR Topside Hull Form with Midship Section

This two-dimensional section was designed and constructed in the Seakeeping Division at NSWCCD [1]. A picture of the experimental test is shown in Figure 6.2. The CFD simulations will mimic the experimental set-up. The CFD simulation will consist of the tumblehome placed in a tank making up three walls, and the fourth representing the atmosphere, shown in Figure 6.3. To see a zoomed-in image of the mesh around the tumblehome, refer to Figure 6.4. The grid spacing is fine around the bilge keels and hull to capture the evolving flow physics as the simulation progresses. The ONR tumblehome is a model-scale ship with principal particulars shown in Table 6.1.

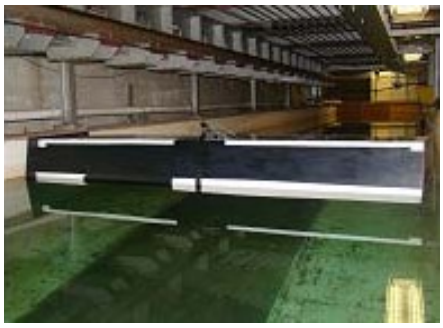

Figure 6.2: DTMB Model #5699-1 in the NSWCCD 140 ft basin

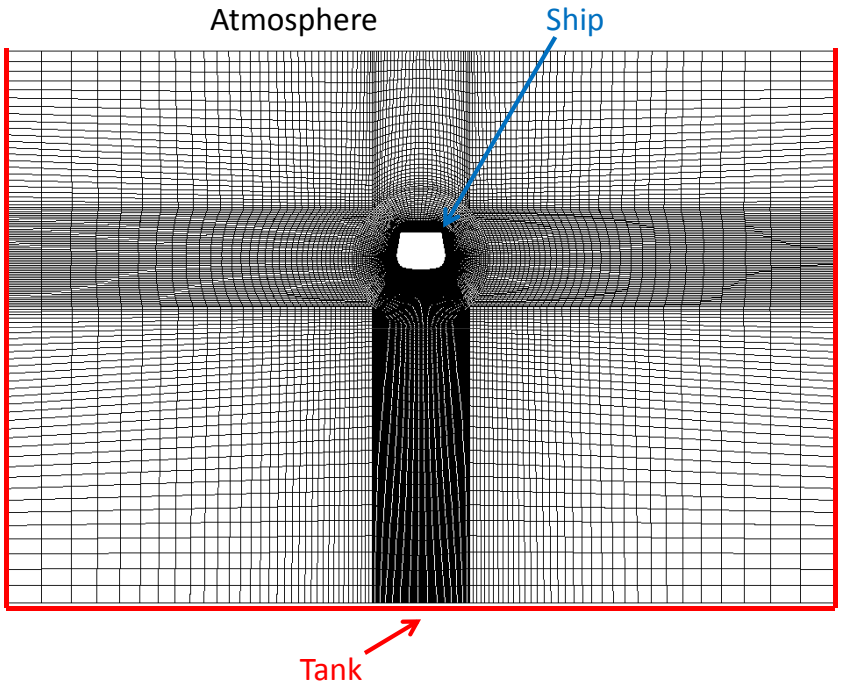

Figure 6.3: Grid Generation of ONR Tumblehome

Effective scale ratio	32
Length, LWL	2.743 m
Calm-waterplane area, A_{WP}	1.588 m^2
Beam, B	0.5875 m
Draft, T	0.172 m
KG	0.172 m
GM	0.132 m
k_{44}/B (with bilge keels)	0.361 (0.366)
Bilge keel span, b_{BK}	0.039 m

Table 6.1: DTMB Model #5699-1 Principal Particulars

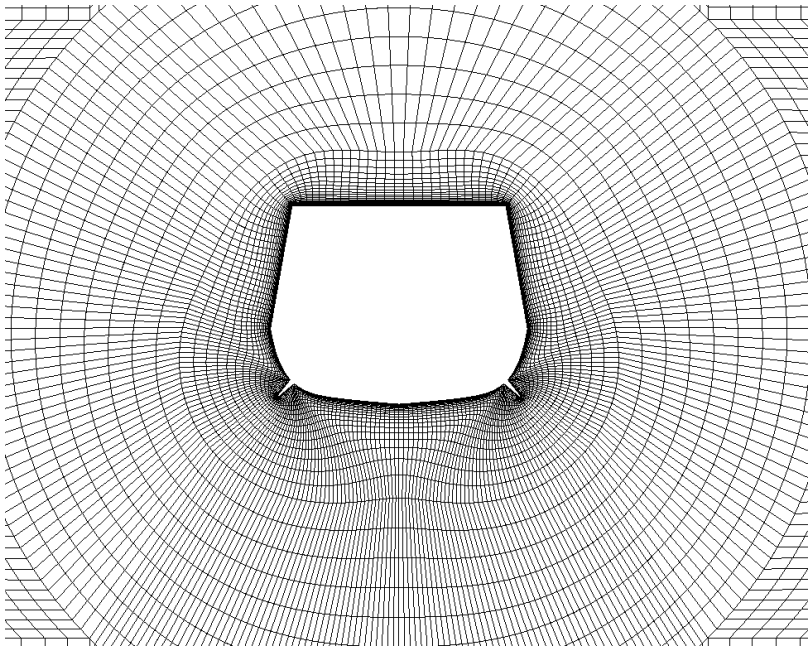

Figure 6.4: Zoomed-In Image of ONR Tumblehome Grid

6.2 Boundary Conditions

Table 6.2 shows the boundary conditions that were used for these computations.

Boundary	Pressure	Velocity
Tank	ZeroGradient	Fixed-Value 0
Atmosphere	Total Pressure	ZeroGradient
FrontAndBack	Empty	Empty
Ship	ZeroGradient	moving Wall (prescribed roll)

Table 6.2: Boundary Conditions for ONR Tumblehome

The ship will be prescribed to roll about its center of gravity, indicated by equation 6.1.

$$\theta = asin(2 \cdot \pi \cdot f \cdot t) \tag{6.1}$$

6.3 Fluid Parameters

The fluid parameters used for these simulations are displayed in Table 6.3.

Viscosity of Water (m^2/s)	$1 \cdot 10^{-6}$
Density of Water (kg/m^3)	1000
Density of Air (kg/m^3)	1

Table 6.3: Fluid Parameters for ONR Tumblehome

6.4 Run Matrix

The run matrix of simulations that will be completed for this thesis are shown in Table 6.4.

Fn	0.0
Roll amplitude (degrees)	15, 30, 45
Roll Frequency (rad/s)	2.17, 2.5, 2.85, 3.81
Bilge Keels	With

Table 6.4: Run Matrix

6.5 Mesh-Motion Techniques

6.5.1 Laplacian Mesh Morphing

The Laplacian mesh morphing transforms the points directly on the moving tumblehome, but skews the cells surrounding the body depending on the degree of rotation. At smaller degrees of rotation, the skewness of the mesh is relatively small and does not alter the solution. However, at large degrees of rotation, the mesh quality does significantly decrease, just as Smith [23] found. Figure 6.5 shows the tumblehome at a roll amplitude of 15°.

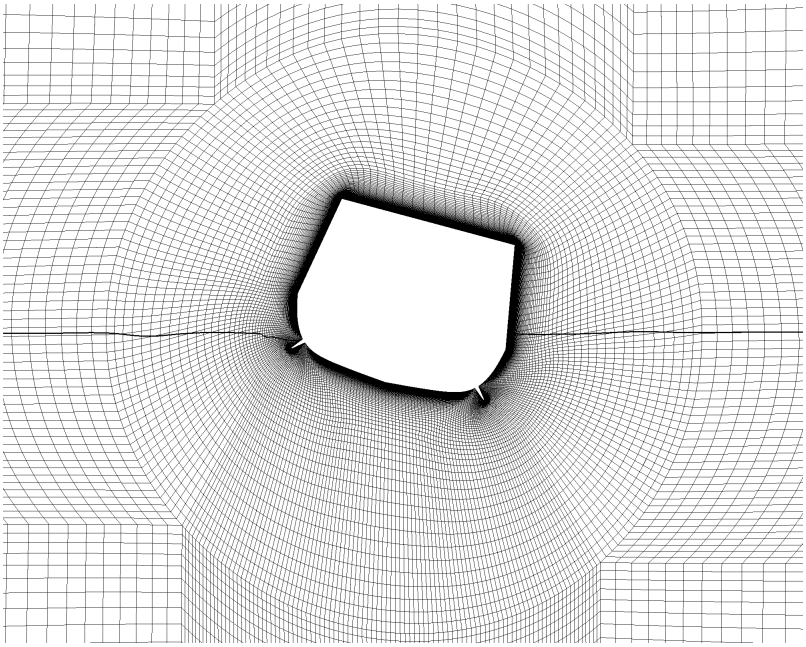

Figure 6.5: Zoomed-In Image of Laplacian Mesh Motion

6.5.2 RBF

The RBF interpolation was found to maintain a high mesh quality near the tumblehome during large rotations as expected. However, it can be demonstrated in Figure 6.6 that cells on the fixed boundaries are highly skewed due to the way the mesh is moved. The inner circular mesh rotates with the tumblehome (Figure 6.7) , but this results in a strange rotation pattern (Figure 6.6) .

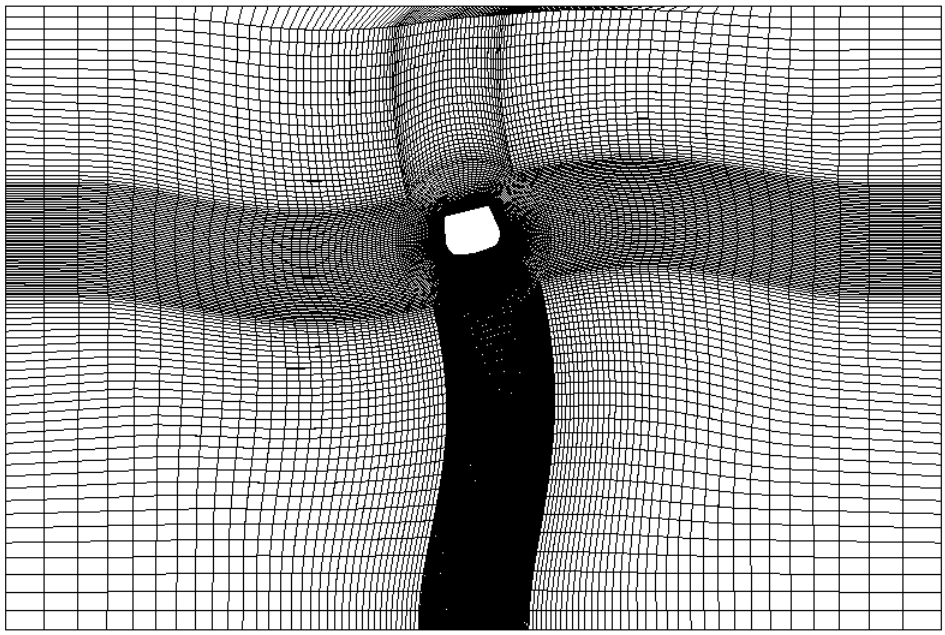

Figure 6.6: RBF Mesh Motion

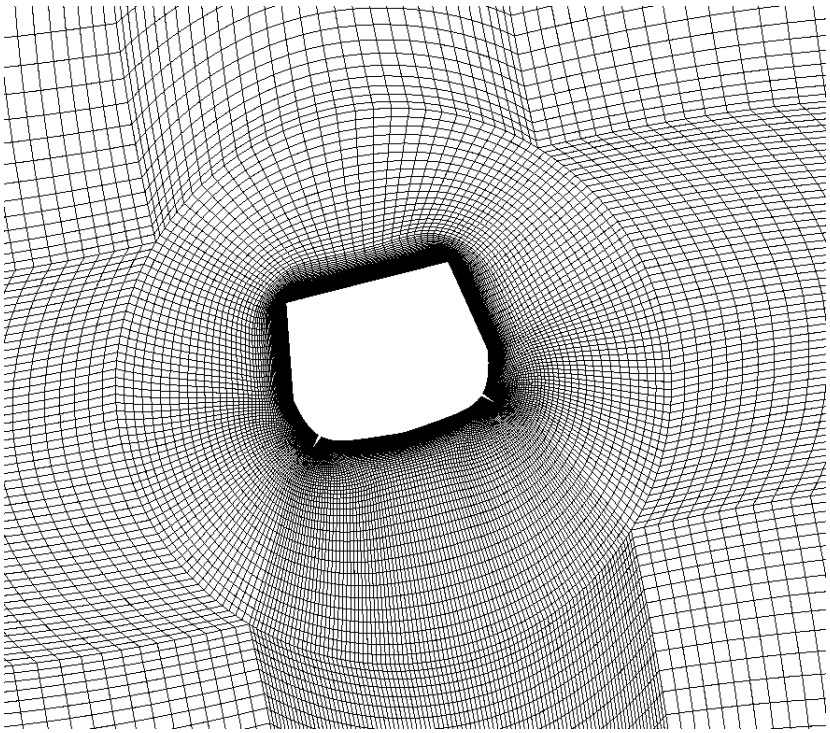

Figure 6.7: Zoomed-In Image of RBF Mesh Motion

6.5.3 GGI

The GGI case has two more boundary conditions that were not discussed in section 6.2, due to the way the mesh motion occurs. Figure 6.8 exposes the inside and outside slider boundary conditions that are not present for any other mesh motion technique. These sliders operate by the outside slider staying fixed with the outer mesh and not being affected by the inner rotational mesh motion. However, the insider slider represents the inner circular mesh and is prescribed to a rotation rate. The inside and outside sliders are touching but do not rely on each other, other than interpolating data across the

interfaces. The non-conformal faces are shown in greater detail by Figure 6.9. In this figure, a zoomed-in image is shown of the inside and outside slider's interface.

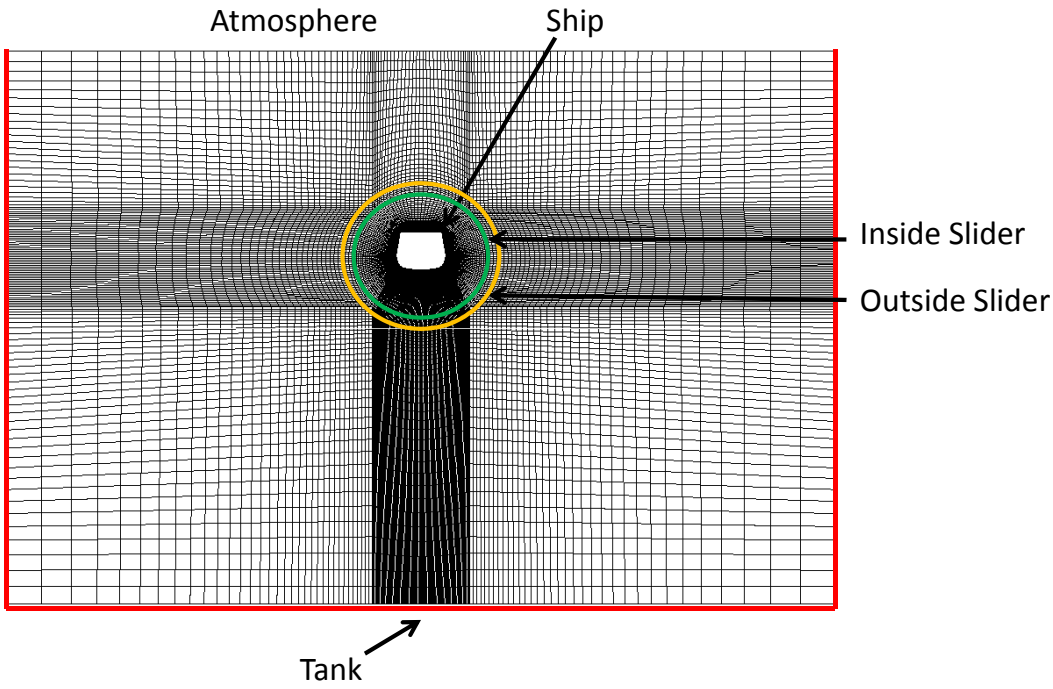

Figure 6.8: GGI Mesh Motion

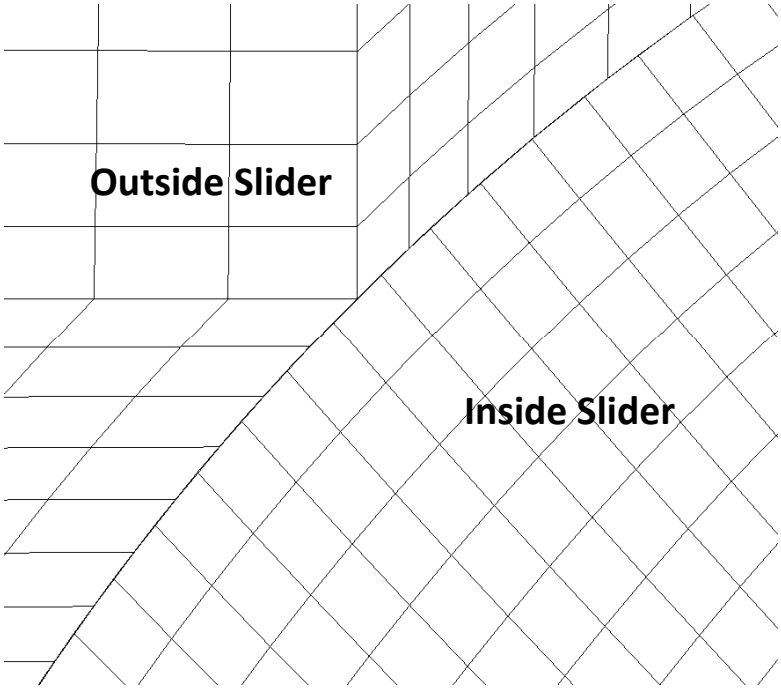

Figure 6.9: Zoomed-In Image of GGI patches

6.5.4 Overset

The initial grid for the overset process is constructed, where two grids overlap each other, shown in Figure 6.10. Through the use of Suggar++ and DiRTlib, the hole points are removed and an overlap minimization is implemented on the grid, resulting in Figure 6.11. As the tumblehome is prescribed to rotation, the overlapped inner grid moves while the outer grid remains fixed. In Figure 6.12, an extreme amplitude case of 45° displays how

the moving grid rotates with the tumblehome. This preserves high mesh quality around the tumblehome and also keeps the far-field grid intact.

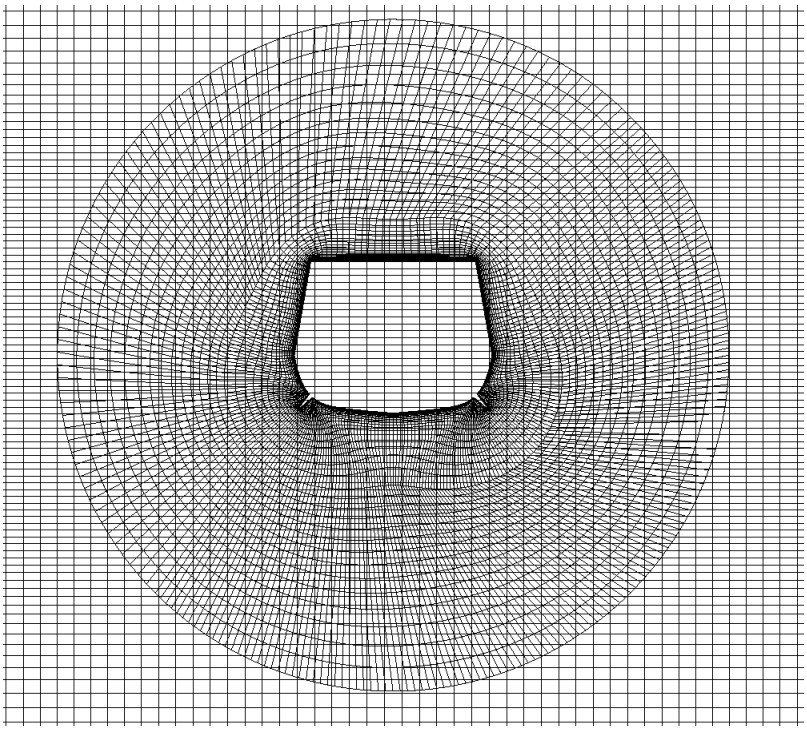

Figure 6.10: Initial Overset Grid

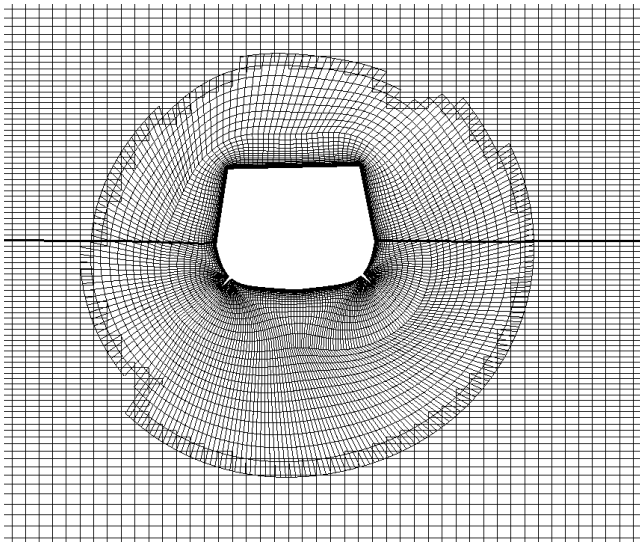

Figure 6.11: Overset Mesh-Motion, No Rotation

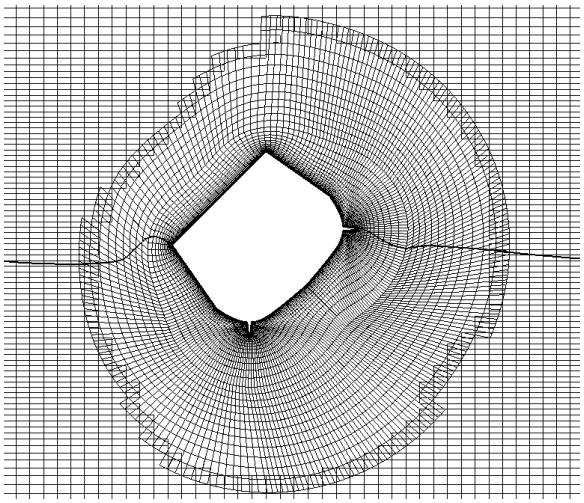

Figure 6.12: Overset Mesh-Motion, Rotated at 45°

6.6 Results

The four mesh-motion techniques were all simulated with the run matrix listed previously in Table 6.4. These techniques will be compared by looking at accuracy, robustness, stability and speed. Table 6.5 compares each technique with the associated time it takes to update the mesh after the tumblehome rotates. From this table, the GGI method is the fastest method. The GGI method is fast because only a fraction of the mesh is moving around the tumblehome, which is why this method is used so frequently in turbomachinery applications. However, the overset method is still relatively fast compared to the other methods. This table explains why the RBF method is not realistic to use for these types of applications, and therefore no results will be shown hereafter. As a reminder, these simulations were only two-dimensional. The RBF scales with number of grid points for 2-D as $4N^3$, and for 3-D as $6N^5$ [3].

Mesh-Motion Technique	Execution Time for Mesh Update
Laplacian	2.1 sec
RBF	40.7 sec
GGI	0.06 sec
Overset	0.12 sec

Table 6.5: Speed Comparison of Mesh-Motion Techniques

The accuracy of the methods will be analyzed by quantifying the forces and moments acting on the ONR tumblehome. Figure 6.13 shows a comparison between overset, GGI, and Laplacian for the unit normal force acting on the bilge keel on the port side of

the ship. As shown in the figure below, GGI and Laplacian methods are very noisy while overset is stable and fairly periodic over several periods. Neither GGI or Laplacian appear to be periodic or show any type of trend over several periods. Results from overset compare closest with the experiment, which will be shown later in this chapter. Figure 6.14 displays the total moment acting on the hull and bilge keels for the three methods. All of the methods give reasonably periodic results over several periods. Unfortunately, none of the three methods accurately predicted the peak value of the moment that the experiment predicted. GGI and Laplacian overestimated, while overset under predicted the total moment compared with the experiment. There could be many reasons for the discrepancy between the computations and experimental results, and this could be an area of future work.

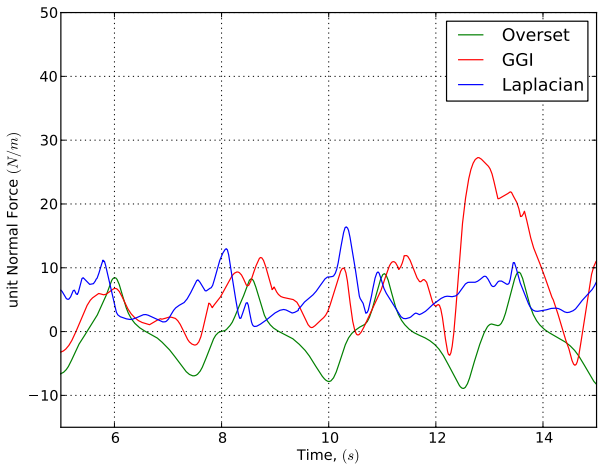

Figure 6.13: unit Normal Force of Bilge Keel on port side, $A = 15^{\circ}$, $\omega = 2.5\,rad/s$

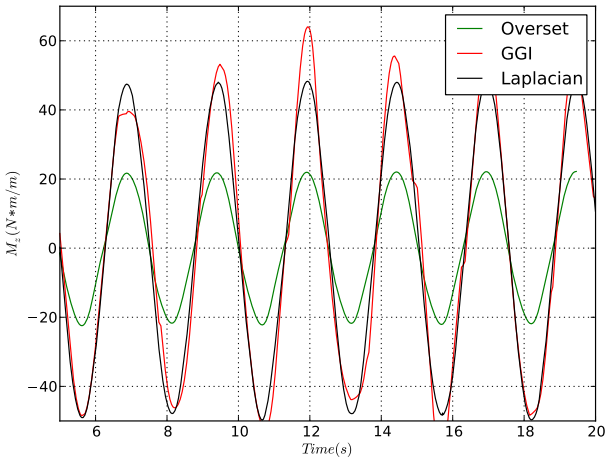

Figure 6.14: Total Moment, $A = 15^{\circ}$, $\omega = 2.5\,rad/s$

6.7 Overset Mesh-Motion Technique

After analyzing the four types of mesh-motion techniques, it was determined that overset is the best dynamic-mesh technique method for multiphase surface-ship hydrodynamics based on speed, robustness and accuracy. Therefore, overset will now be compared with the experimental data that was collected by Bassler for large amplitude roll motion [1].

There are several steps that were followed to ensure a proper solution was attained for the overset method. First, Figure 6.15 displays the limit-cycle, for the overset method, of both bilge keels. These results are a good indication that stability has been reached.

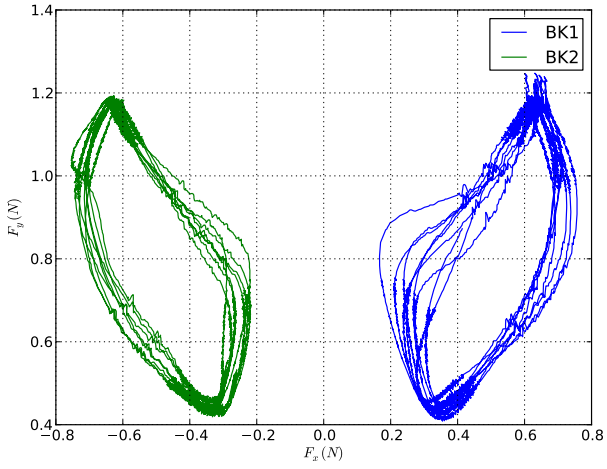

Figure 6.15: Limit-Cycle for Bilge Keels

The next feature to examine is the flow physics around the tumblehome during a period of roll. Figure 6.19 displays a roll cycle for one period of the simulation. There are many

features of the flow physics that need to characterized. First, when the bilge keels emerge from the free-surface, "water shipping" does occur as Bassler also observed [1]. When the bilge keel re-enters the water, entrainment of air occurs at the underside of the bilge keel. Vortex shedding of the air is shown from the second to third frame in the Figure 6.19. In the fourth frame, a wave is formed at the free-surface. Similar characteristics can be seen for both bilge keels during one roll cycle.

Computational results and experimental data of the unit normal force on a bilge keel was compared. The CFD over predicts the force acting on a bilge keel compared to the experimental results, shown in Figure 6.16. The smallest amplitude CFD case compares closest with the experimental data. The larger amplitude cases, shown in Figures 6.17 and 6.18 do not compare well. The flow physics observed are similar, however, it is not understood why the unit normal force data is not matching.

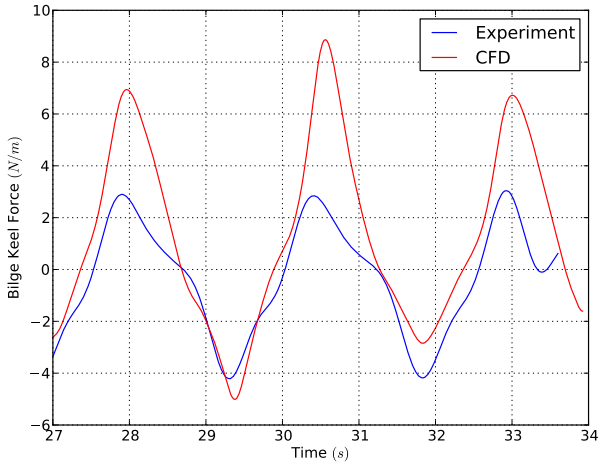

Figure 6.16: Bilge Keel Unit Force for Starboard Side, $A = 15^{\circ}$, $\omega = 2.5\,rad/s$

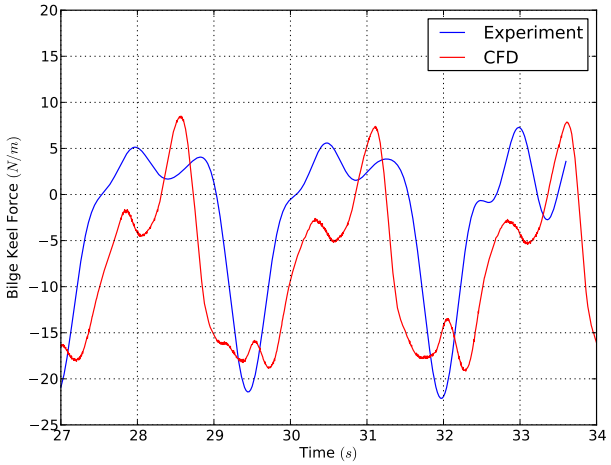

Figure 6.17: Bilge Keel Unit Force for Starboard Side, $A = 30^{\circ}$, $\omega = 2.5\,rad/s$

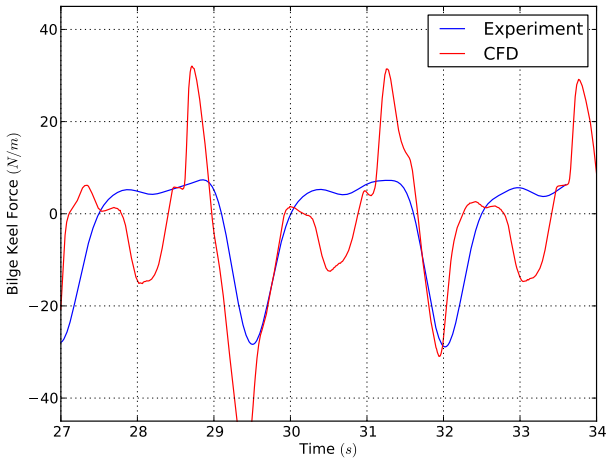

Figure 6.18: Bilge Keel Unit Force for Starboard Side, $A = 40^{\circ}$, $\omega = 2.5\,rad/s$

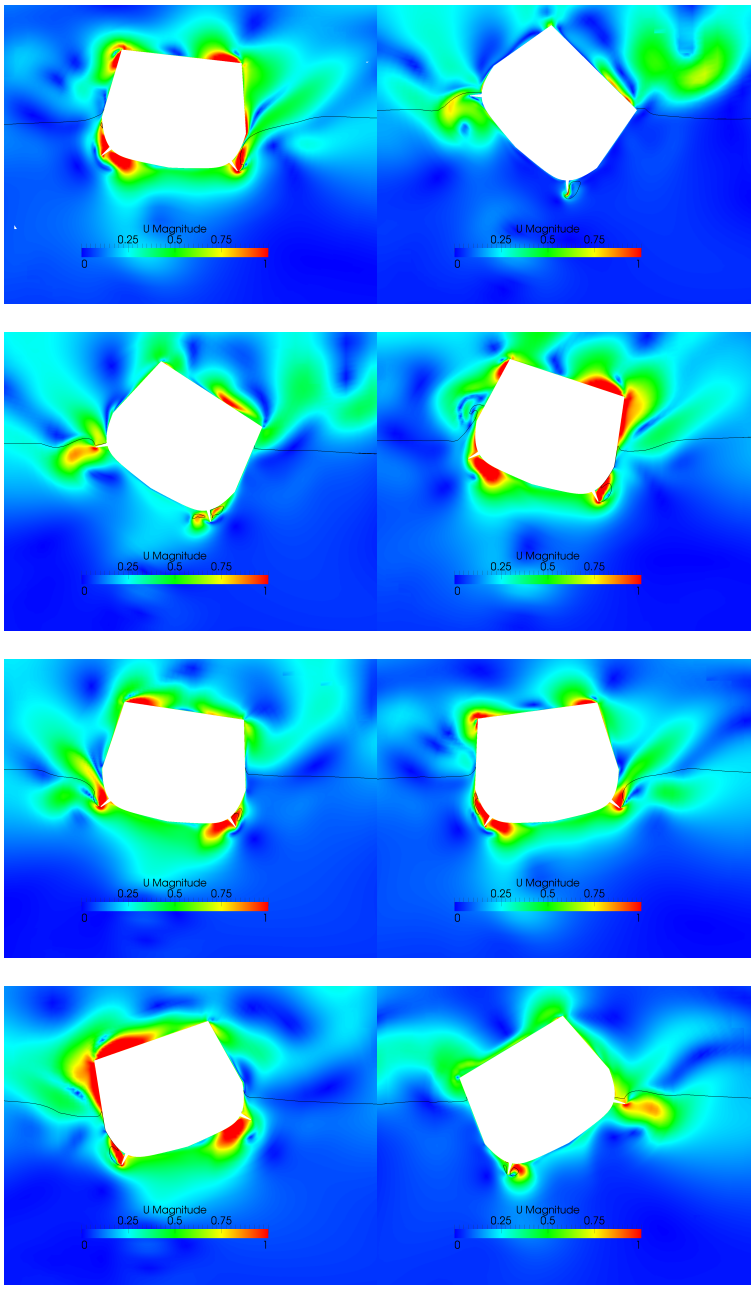

Figure 6.19: Tumblehome Roll Cycle, $A = 45^{\circ}$, displaying Velocity Magnitude

Chapter 7

Summary

CFD simulations of dynamically moving ship-hull sections with sharp bilge keels in a viscous fluid was studied in this thesis. Steady and unsteady boundary layer flows for a flat plate and ship-hull geometry were of particular interest in this work. k-ϵ and Spalart-Allmaras turbulence models were compared using OpenFOAM for steady boundary layer flows on a flat plate geometry. This verified that the Spalart-Allmaras turbulence model and OpenFOAM were sufficient in capturing the viscous sublayer, buffer layer and log-layer of the boundary layer. Unsteady boundary layer flows were examined, beginning with Stokes second problem. The oscillation of a flat plate resembles the rolling motion of a ship, which is why this problem was modeled. The analytic and computational results were in good agreement for all time steps considered. This further validated the use of OpenFOAM by establishing that the velocity distribution is capturing an oscillating flow. The final flat plate verification study was oscillatory free-stream flow. This flow was more complex due to the velocity over shoots and phase lags present. The Blasius solution is a self-similar solution and was compared to the U_{mean} value in the CFD simulations. There was good agreement. In particular, the phase lags and small-amplitude velocity overshoots in the boundary layer were captured.

Keulegan-Carpenter flow was the next verification study performed. It involved unsteady boundary layer flow over ship-hull sections with an oscillatory free-stream flow. This

study provided better insight into oscillatory boundary layer flows for model-scale and full-scale ship-hull sections. A Fourier analysis was completed and the Fourier coefficients for model-scale and full-scale collapsed for two different ship-hull sections analyzed. The conclusion drawn in this chapter was that the introduction of bilge keels cause the force due to drag compared to inertia to increase with an accelerated flow.

Studying unsteady boundary layer flows due to roll motion in a viscous fluid is challenging. Four types of dynamic-meshing techniques were analyzed for full-scale ship-hydrodynamic applications. These methods include Laplacian, GGI, RBF and overset. The Laplacian method was robust but gave noisy and non-periodic forces. GGI was the fastest method studied at updating the mesh between time-steps but also gave noisy results similar to the Laplacian method. RBF proved to be too computationally expensive, and therefore no results were shown. After four dynamic mesh-motion techniques were analyzed, overset was determined to be superior based on speed, robustness, and stability. Overset is by far the most general technique for complex geometries and motions.

The overset method was then analyzed further and compared with recent experimental results. A limit-cycle study was completed to prove stability of this method, and the flow physics were evaluated in detail. The expected flow physics were observed, such as vortex-shedding, air entrainment and "water shipping." However, the computational results and experimental data do not agree. At lower amplitudes, similar forces were seen, but at higher amplitudes, there is very little similarity in the comparisons.

There is an area of future work that has evolved from this thesis. Even though four types of dynamic-mesh techniques were analyzed, and overset proved to be superior, there is

a discrepancy with the experimental data. This discrepancy needs to be resolved. This thesis evaluated single DOF motion, but this type of flow is not realistic. Six DOF motion in forward speed with three-dimensions is more applicable to real world naval-hydrodynamic problems.

Bibliography

[1] Christopher Bassler, Arthur Reed, and Alan Brown. Characterization of physical phenomena for large amplitude ship roll motion. In *The 29th American Towing Tank Conference*, 2010.

[2] M. Beaudoina and H. Jasak. Development of a Generalized Grid Interface for Turbomachinery simulations with OpenFOAM. Open Source CFD International Conference, 2008.

[3] Frank Martijn BOS. *Numerical simulations of flapping foil and wing aerodynamics.* PhD thesis, 2009.

[4] Christopher E. Brennen. *Fundamentals of Multiphase Flows.* Cambridge University Press, 2005.

[5] USS ARLEIGH BURKE.

[6] Naval Surface Warfare Center Carderock Division. Surface ship model 5415.

[7] P.M. Carrica, R.V. Wilson, R.W. Noack, and F. Stern. Ship motions using single-phase level set with dynamic overset grids. *Computers and Fluids*, 36(9):1415–1433, 2007.

[8] JE Choi, MK Sreedhar, and F. Stern. Stokes layers in horizontal-wave outer flows. *Journal of Fluids Engineering*, 118(3), 1996.

[9] Bangun EP, Wang CM, and Utsunomiya T. Hydrodynamic forces on a rolling barge with bilge keels. *Applied Ocean Research*, 32:219–232, 2010.

[10] JH Ferziger and M. Peric. *Computational Methods for Fluid Dynamics. 2002.* Springer.

[11] Y. Himeno. Prediction of Ship Roll Damping. A State of the Art. pages 1–16, 1981.

[12] Y. Ikeda. Prediction methods of roll damping of ships and their application to determine optimum stabilization devices. *Marine Technology*, 41(2):89–93, 2004.

[13] T. Javaherchi. Review of Spalart-Allmaras Turbulence Model and its Modifications. pages 1–13, 2010.

[14] P.K. KUNDU and I.M. COHEN. Fluid mechanics. 2008.

[15] WB Morgan and WC Lin. Predicting ship hydrodynamic performance in today's world. *Naval Engineers Journal*, 110(5):91–98, 1998.

[16] R. Noack. SUGGAR: a general capability for moving body overset grid assembly. *AIAA paper*, 5117, 2005.

[17] Ralph Noack, David Boger, Robert Kunz, and Pablo Carrica. Suggar++: An improved general overset grid assembly capability. *19th AIAA Computational Fluid Dynamics Conference*, June 2009.

[18] Ralph W. Noack. Dirtlib: A library to add an overset capability to your flow solver. In *17th AIAA Computational Fluid Dynamics Conference*, 2006.

[19] T. Perez, T.I. Fossen, and A. Sorensen. A discussion about seakeeping and manoeuvring models for surface vessels. *NTNU, TechReport MSS-TR-001*, page 10, 2004.

[20] I. RA and G. IM. Modeling of Ship Roll Dynamics and Its Coupling with Heave and Pitch. *Mathematical Problems in Engineering*, 2010, 2009.

[21] T. Sarpkaya. Force on a circular cylinder in viscous oscillatory flow at low Keulegan—Carpenter numbers. *Journal of Fluid Mechanics*, 165:61–71, 1986.

[22] S.E. Sherer and J.N. Scott. High-order compact finite-difference methods on general overset grids. *Journal of Computational Physics*, 210(2):459–496, 2005.

[23] Kevin R. Smith. Computation of viscous multiphase hydrodynamics and ship motions during wave-slap events and wave excited roll. Master's thesis, The Pennsylvania State University, 2009.

[24] Demetri P. Telionis. *Unsteady Viscous Flow*. Springer-Verlag New York Inc., 1981.

[25] M. Hughes W. Belknap, C. Bassler. Comparisons of body-exact force computations in large amplitude motion. *28th Symposium on Naval Hydrodynamics*, 2010.

[26] M. E. Crawford W. M. Kays. *Convective Heat and Mass Transfer*. McGraw-Hill, Inc., third edition, 1993.

[27] F.M. White. *Viscous Fluid Flow*. McGraw-Hill, 1974.

[28] D.C. Wilcox. *Turbulence modeling for CFD*. DCW industries La Canada, CA, 2006.

[29] A.M. Wissink, J. Sitaraman, V. Sankaran, D.J. Mavriplis, and T.H. Pulliam. A Multi-Code Python-Based Infrastructure for Overset CFD with Adaptive Cartesian Grids. *AIAA Paper*, 927:2008, 2008.

[30] RW Yeung, D. Roddier, SW Liao, B. Alessandrini, and L. Gentaz. On roll hydrodynamics of cylinders fitted with bilge keels. pages 863–880, 2001.